Uncertainty Analysis of Digital Elevation Models by Spatial Inference From Stable Terrain

Romain Hugonnet, Fanny Brun, Etienne Berthier, Amaury Dehecq, Erik Schytt Mannerfelt, Nicolas Eckert, and Daniel Farinotti

***Abstract*—The monitoring of Earth's and planetary surface elevations at larger and finer scales is rapidly progressing through the increasing availability and resolution of digital elevation models (DEMs). Surface elevation observations are being used across an expanding range of fields to study topographical attributes and their changes over time, notably in glaciology, hydrology, volcanology, seismology, forestry, and geomorphology. However, DEMs frequently contain large-scale instrument noise and varying vertical precision that lead to complex patterns of errors. Here, we present a validated statistical workflow to estimate, model, and propagate uncertainties in DEMs. We review the state-of-the-art of DEM accuracy and precision analyses, and define a conceptual framework to consistently address those. We show how to characterize DEM precision by quantifying the heteroscedasticity of elevation measurements, i.e., varying vertical precision with terrain- or sensor-dependent variables, and the spatial correlation of errors that can occur across multiple spatial scales. With the increasing availability of high-precision observations, our workflow based on independent elevation data acquired on stable terrain can be applied almost anywhere on Earth. We illustrate how to propagate uncertainties for both pixel-scale and spatial elevation derivatives, using terrain slope and glacier volume changes as examples. We find that uncertainties in DEMs are largely underestimated in the literature, and advocate that new metrics of DEM precision are essential to ensure the reliability of future land elevation assessments.**

Manuscript received 23 March 2022; revised 10 June 2022; accepted 27 June 2022. Date of publication 6 July 2022; date of current version 17 August 2022. *(Corresponding author: Romain Hugonnet.)*

Romain Hugonnet is with the LEGOS, Université de Toulouse, CNES, CNRS, IRD, UPS, 31000 Toulouse, France and the Laboratory of Hydraulics, Hydrology and Glaciology (VAW), ETH Zürich, 8049 Zürich, Switzerland, and also with the Swiss Federal Institute for Forest, Snow and Landscape Research (WSL), 8903 Birmensdorf, Switzerland (e-mail: romain.hugonnet@gmail.com).

Fanny Brun is with the IGE, Université Grenoble Alpes, CNRS, IRD, Grenoble INP, 38058 Grenoble, France (e-mail: fanny.brun@univ-grenoble-alpes.fr).

Etienne Berthier is with the LEGOS, Université de Toulouse, CNES, CNRS, IRD, UPS, 31000 Toulouse, France (e-mail: etienne.berthier@legos.obs-mip.fr).

Amaury Dehecq is with the Laboratory of Hydraulics, Hydrology and Glaciology (VAW), ETH Zürich, 8049 Zürich, Switzerland and the Swiss Federal Institute for Forest, Snow and Landscape Research (WSL), 8903 Birmensdorf, Switzerland, and also with IGE, Université Grenoble Alpes, CNRS, IRD, Grenoble INP, 38058 Grenoble, France (e-mail: amaury.dehecq@univ-grenoble-alpes.fr).

Erik Schytt Mannerfelt and Daniel Farinotti are with the Laboratory of Hydraulics, Hydrology and Glaciology (VAW), ETH Zürich 8049 Zürich, Switzerland, and also with the Swiss Federal Institute for Forest, Snow and Landscape Research (WSL), 8903 Birmensdorf, Switzerland (e-mail: mannerfelt@vaw.baug.ethz.ch; daniel.farinotti@ethz.ch).

Nicolas Eckert is with the Université Grenoble Alpes, INRAE, UR ETNA, 38402 Grenoble, France (e-mail: nicolas.eckert@inrae.fr).

This article has supplementary downloadable material available at https://doi.org/10.1109/JSTARS.2022.3188922, provided by the authors.

Digital Object Identifier 10.1109/JSTARS.2022.3188922

***Index Terms*—Error propagation, Geostatistics, Random, Remote sensing, Surface height, Systematic, Variogram.**

I. Introduction

DIGITAL elevation models (DEMs) are gridded, numerical representations of surface elevation. DEMs have a long history of interpolation from point measurements and digitized historical maps [1], [2]. Nowadays, DEMs are mostly generated from radar interferometry [3], [4], optical stereophotogrammetry [5], [6], or laser scanning [7], [8] of a planetary surface. When produced from these remote sensing techniques, DEM grid cells essentially represent surface elevation observations timestamped to the date of instrument acquisition. With the ever-improving coverage and precision of satellite and airborne sensors [9], land surface assessments based on DEMs are advancing toward estimates that are both more spatially and more temporally resolved [10], [11]. Additionally, the recent unlocking of historical optical archives has created unprecedented potential for studying half a century of Earth's surface elevation [12]–[14].

Studies that harness elevation observations can generally be divided into two groups. The first group relies on single-acquisition and often gap-filled DEMs to extract essential topographic characteristics, e.g., in river discharge and flood modeling [15]–[17], geomorphological terrain analysis [18]–[21], tectonic monitoring [22]–[25], avalanche risk prediction [26], land classification [27], [28], onshore inundation and sea-level rise forecasting [29]–[31], and planetary surface characterization [32], [33]. The second group requires multiple acquisitions to study surface elevation changes over time, e.g., for landslide and rock avalanche detection [34]–[36], seasonal snow depth assessment [37]–[39], lava flow volume quantification [40], [41], canopy height evolution [42]–[44], and glacier, ice sheet and ice shelf mass balance estimation [45]–[47]. In both groups, and for all applications, the interpretation of results and its robustness are inextricably intertwined with the accuracy and precision of the underlying DEMs.

Accuracy and precision are related to systematic and random errors. In the case of DEMs, they have been the focus of specific research [48]–[51], software development [52], and questioning [53]–[56] since the beginning of the numerical era. Yet, these efforts are dwarfed by the tremendous increase of studies that rely on DEMs [57] and the processing of ever larger data volumes [58]–[60]. Most critically, the analysis of many modern

studies is still confined to simplified metrics for accuracy and precision that mix systematic and random errors (e.g., [61]–[63]) and fail to describe the strong spatial variations and correlations in errors observed in DEMs (e.g., [64]–[66]).

Here, we present a statistical workflow to robustly estimate and propagate uncertainties in DEMs; most specifically, we:

1) perform a literature review of analyses dealing with DEM accuracy and precision;
2) propose a framework based on spatial statistics to consistently address DEM accuracy and precision;
3) present robust inferential methods to estimate elevation heteroscedasticity and spatial correlation of errors;
4) analyze the impact on the uncertainty of elevation derivatives with terrain slope and glacier volume changes;
5) provide access to our methods through the open, tested, and documented Python package xDEM.

II. Literature Review

A. Mitigating Poor DEM Accuracy Before Studying Precision

The term accuracy has been used to describe either systematic errors or, in some instances, both systematic and random errors, leading to some confusion. In the present article, we define accuracy as the description of systematic errors only, also known as "trueness" [67], which is related to elevation biases. Poor accuracy is common in DEMs and has been a major source of error in land elevation assessments, particularly during the advent of space-borne DEMs. Limitations in instrument positioning, orientation, or postprocessing often lead to erroneous horizontal referencing [66], [68], vertical shifts [69], [70], or tilts [71], [72] that propagate into elevation biases [see Fig. 1(a)]. By utilizing terrain with elevation assumed stable over time, methods performing three-dimensional alignment of DEMs have flourished, relying on either generic registration methods [73]–[75], least squares approaches [71], [76] or specifically developed DEM registration based on terrain constraints [77], [78]. These methods proved robust for aligning a DEM either to an external reference DEM, or to accurate geolocated point elevation data such as space-borne laser altimetry [79], [80].

The above registration methods are only successful at correcting elevation biases common to the entire DEM grid, however. Other biases remain present once 3-D alignment is attained and can arise from resolution [81], [82], specific image deformations, and instrument biases [13], [66] or physical properties of the observed terrain such as radar penetration into snow and ice [83], [84] or into forest canopy [43]. Most of these biases are instrument- or application-dependent and, therefore, require specific considerations. Notwithstanding those, poor DEM accuracy has been largely addressed by the robustness of registration methods that have become increasingly widespread, thereby shifting the focus towards the next limiting factor: better quantifying DEM precision.

B. Inherent Variability of Vertical Precision

Precision describes random errors [67] and is related to elevation measurement variance. One aspect of DEM precision consists of the pixel-scale dispersion of elevations that we refer to as "vertical precision." DEMs are generated from acquisitions that possess intrinsic, random measurement errors. At the pixel scale, instrument resolution, spectral range, and encoding depth of optical sensors directly affect the quality of stereo-correlation [5], [6], [85], radar slant angle, and height of ambiguity play an important role in interferometric coherence [86], [87] while laser wavelength, sunlight background radiation, target reflectivity, and backscattering properties modulate laser signal-to-noise ratio [88], [89]. Many instrument- or processing-related metrics constitute quality indicators of the estimated elevations. These indicators have been almost exclusively used for the filtering of observations of lesser quality, however, and only occasionally as a tool toward improved modelling of sensor-specific variability in vertical precision (e.g., [90]).

Besides, the geometry of instrument acquisition can exacerbate random errors depending on the relief of the observed landforms [see Fig. 1(a)]. Vertical precision has indeed been long shown to decrease with terrain slope [48], [91]–[94]. Several assessments account for this variability by partitioning the elevation variance into categories of flat and steep terrain (e.g., [59]). Most studies use a single metric to describe vertical precision, however, often reporting a standard deviation (e.g., $\pm$ 2 m). Such simple metrics are insufficient in describing the heteroscedasticity of elevation measurements, i.e., the variability in vertical precision. Although some studies quantified and modeled this heteroscedasticity [64], [95], [96], this modeling was generally performed without validation of the underlying methodology and, most critically, without considering the effect of spatial correlations.

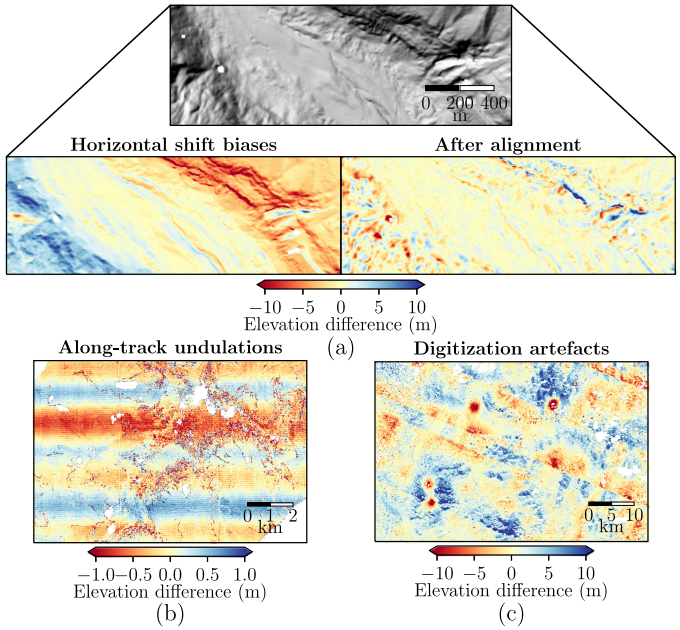

Fig. 1. Patterns of errors in DEMs. (a) Elevation differences of horizontal shifts (left) and after alignment (right) with terrain hillshade (top), from the DEMs in Table I. The horizontal shift between Pléiades and SPOT-6 DEMs is of 2 m east and 4 m north, creating large biases despite being relatively small (half a pixel). (b)–(c) Noise owed to (b) along-track undulations in a Pléiades–Pléiades DEM difference and to (c) digitization artefacts in a KH-9–ArcticDEM DEM difference [13], after alignment.

C. Correlated Noises That Plague DEMs

Another aspect of DEM precision concerns the interpixel spatial dependency of random errors, here referred to as "spatial correlations." Spatial correlations describe structures of noise that show a location-dependent pattern, which can often be traced back to limitations during acquisition or postprocessing. Along-track undulations have been observed in many DEMs generated from air- and space-borne sensors [see Fig. 1(b)], including the Advanced Spaceborne Thermal Emission and Reflection Radiometer (ASTER) [47], [66], the Satellite Pour l'Observation de la Terre (SPOT) [97], [98], Pléiades [39], [99], and the Shuttle Radar Topography Mission (SRTM) [58], [100], [101] [see Fig. S1]. Processing noise is common in DEMs requiring image digitization including aerial photographs [102], [103] or historical satellite imagery such as Hexagon KeyHole-9 (KH-9) [13], [104] [see Fig. 1(c)]. To mitigate these correlated noises, DEM correction methods have emerged [82], [105] but are still burgeoning for specific types of errors [66], [106], [107], and their performance is highly dependent on the type of terrain.

Furthermore, nearly all DEMs contain structural short-range correlation of errors. The degree to which a DEM grid spacing represents its native resolution [108], [109] and how that resolution has possibly been degraded through interpolation [110] determine the severity of these short-range correlations. When upsampled to a larger grid spacing, vertical precision improves directly as a function of the underlying spatial correlations [111]. Spatial correlations are generally quantified using an empirical variogram [112], [113] estimated either on the basis of differences with independent elevation observations [2], [114] or those with simulated elevation surfaces [115], [116]. Many studies have used variograms, but have almost exclusively used short range models (i.e., 5–20 times the pixel size). Few studies modeled long-range correlations, that is, correlations that persist over distances several orders of magnitude larger than the pixel size [13], [47], [65]. The widespread occurrence of long-range noise in DEMs thus constitutes a critical limitation in the analysis of DEM precision, and one that directly affects uncertainty propagation.

D. Uncertainty Propagation to Elevation Derivatives

To propagate elevation variance into uncertainties of elevation derivatives (i.e., variables that are derived from elevations), a large set of methods has been applied that generally relies on spatial statistics. Spatial statistics, also known as geostatistics [112], [113], [117], provide a large body of theories and methods that, among others, can address spatial uncertainty analyses [118]–[120] by characterizing spatial correlations that depend only on the distance between observations. These uncertainty propagation methods can be subdivided into two groups: 1) Monte Carlo techniques that simulate multiple random realizations of correlated error fields [121]–[123], notably including Sequential Gaussian simulation [117] and Fourier randomization [124]; and 2) gradient techniques that analytically approximate the variance of a derivative through simplified equations, that can be either based on Taylor series expansion [121] for any derivative of elevation, or approximations of variogram integration [65] for spatial derivatives.

The first group has been widely used for topographic variables, notably in hydrology [16], [57], [125], [126] and occasionally for spatial derivatives in glaciology [127]. The second group is used less frequently, both for Taylor series expansions developed in few applications [128]–[131], and for variogram integration implemented mainly in glaciology and geomorphology [65], [132]. Although both groups are expected to perform similarly, Monte Carlo techniques are computationally expensive, especially at fine resolution. Analytical approximations, instead, require a theoretical description of variance propagation that can reach a high degree of complexity for some derivatives [133]. To our knowledge, few studies [132] constrained these propagation methods with estimates of heteroscedasticity and spatial correlation of errors into a single framework for DEMs, and none tested the underlying assumptions of spatial statistics. In the following, we propose such a framework, and later describe methods to robustly estimate its key components.

III. Problem Formulation

A. Elevation Bias and Variance at Each Location

We consider the elevation observation $\hat{h}(x,y,t)$ located at (x,y) in space and t in time, and pertaining to the DEM $\mathcal{D}$. Annotating the true unknown elevation at the same location $h(x,y,t)$, we can state that the elevation observation has a bias $\delta h(x,y,t)$ if, over a large number of repeated measurements $i \in \mathcal{I}$ of elevation $\hat{h}(x,y,t)_i$ at (x,y,t), we have

$$\overline{\hat{h}(x,y,t)_i|_{\mathcal{I}}} - h(x,y,t) = \delta h(x,y,t). \tag{1}$$

The repeat elevation measurements around the bias $\delta h(x,y,t)$ are subject to random measurement errors $\epsilon_h(x,y,t)$ with variance $\sigma_h^2(x,y,t)$, whose distribution is not necessarily normal and might depend on time and location:

$$\hat{h}(x,y,t) = h(x,y,t) + \delta h(x,y,t) + \epsilon_h(x,y,t). \tag{2}$$

In practice, acquiring a large number of repeat measurements at both the same location and time is not feasible, and we therefore turn toward inferential methods to estimate these biases and variance.

B. Inference From Stable Terrain

DEMs benefit from a great asset, largely uncommon to other remote sensing data, which is that large proportions of planetary surface elevations remain virtually unchanged through time. In fact, elevation changes caused by erosion, short vegetation growth, or continental drift are typically small compared to the precision of the measurement. Terrains such as bare rock or grasslands—later referred to as "stable terrain"—thus provide the means of analyzing multiple elevation measurements acquired at different points in time as if they were acquired from simultaneous measurements $\hat{h}(x,y,t)_i$:

$$\frac{dh(x,y,t)}{dt} \approx 0 \text{ for } (x,y) \in \text{stable terrain}. \tag{3}$$

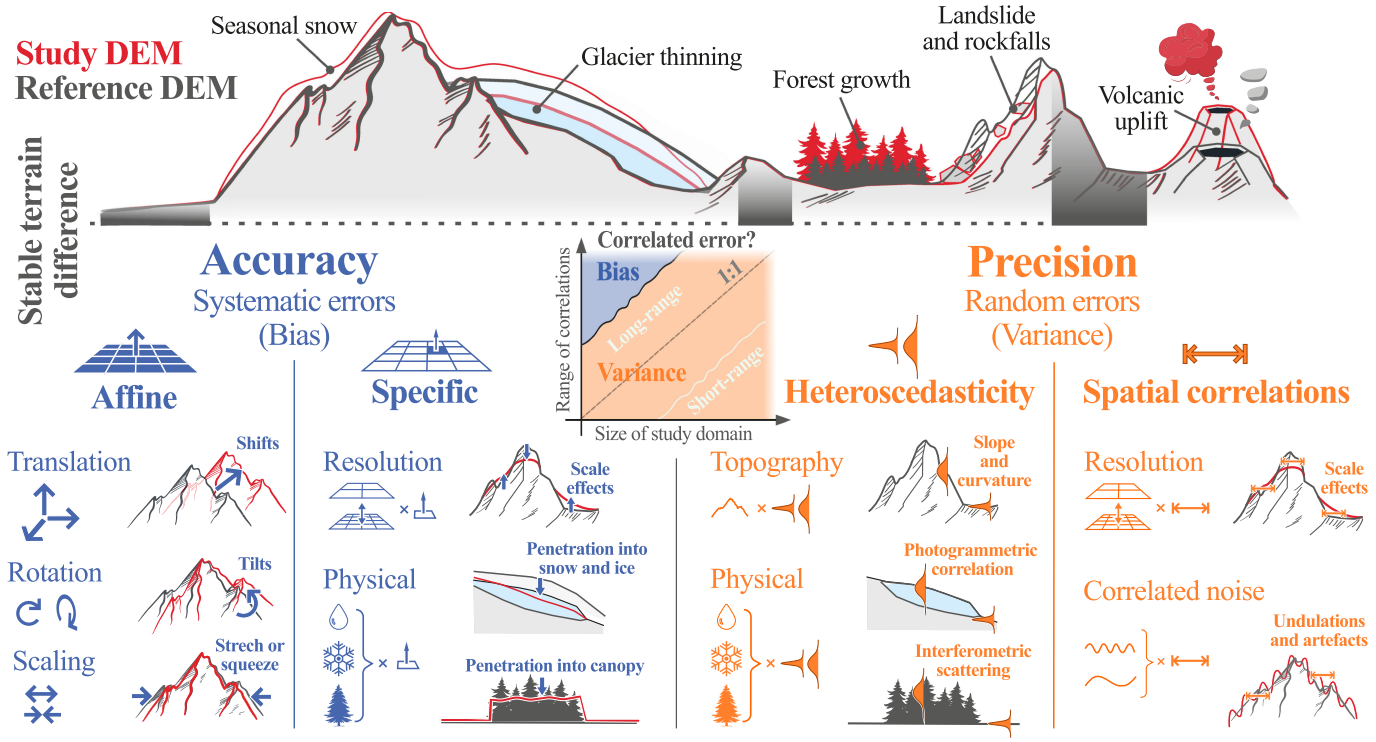

Fig. 2. Framework for uncertainty analysis of DEMs. Analysis of accuracy and precision by spatial inference from stable terrain, with accuracy divided into affine and specific biases (see Section III-C), and precision divided into heteroscedasticity and spatial correlation of errors (see Section III-F).

While this temporal consistency unlocks the potential to analyze elevation acquisitions independently of time t, it is impeded by the number of required DEMs. For each location (x, y), the number of samples to perform the statistical analysis would always be at best equal to the total number of independent acquisitions, requiring a large number of DEMs. Therefore, we investigate the spatial properties of elevation biases and variance.

C. Spatial Homogeneity After Affine Alignment

Elevation biases and variance are inherent to instrumental limitations, to the physical properties of the observed terrain, as well as its topography (see previous Sections II-A—II-B). Among many types of location-specific biases, a general exception is that of grid misalignment to the true elevations $h(x, y, t)$ that follows specific geometric distributions linked to the gridded nature of DEMs [see Fig. 1(a)]. In our framework, we therefore split elevation biases into two categories: affine biases $\delta h_{\mathcal{A}}$ that are common to the entire DEM (e.g., translation, rotation, scaling), and nonaffine "specific" biases $\delta h_{\mathcal{S}}$ that occur at the grid cell level and vary with instrumental and topographical effects [see Fig. 2]:

$$\delta h(x, y, t) = \delta h_{\mathcal{A}}(x, y, t) + \delta h_{\mathcal{S}}(x, y, t). \quad (4)$$

Once an alignment is attained by the affine transformation $\mathcal{A}$ giving $\mathcal{A}(x, y, t) = \delta h_{\mathcal{A}}(x, y, t)$, we assume that, for a single DEM $\mathcal{D}$, specific elevation biases $\delta h_{\mathcal{S}}$ and elevation variance σ_h^2 have a spatial distribution that is homogeneous with the properties of the instrument and the observed terrain $\mathcal{P}$. We use this spatial homogeneity to substitute space for time. For example, we consider that elevations $h(x_1, y_1, t)$ and $h(x_2, y_2, t)$ of $\mathcal{D}$ acquired on the same surface type (e.g., bare rock), and under the same topographical attributes (e.g., flat) will have similar specific biases and variance

$$\left.\begin{array}{l} \delta h_{\mathcal{S}}(x_1, y_1) \approx \delta h_{\mathcal{S}}(x_2, y_2) \\ \sigma_h(x_1, y_1) \approx \sigma_h(x_2, y_2) \end{array}\right\} \text{for } \mathcal{P}(x_1, y_1) = \mathcal{P}(x_2, y_2). \quad (5)$$

Combining the assumptions of (3) and (5), and provided that we describe all the properties $\mathcal{P}$ of spatial homogeneity, a large sample size can be used to infer δh and σ_h at each location (x, y) from a single difference between a DEM and an independent source of elevation data. The properties of spatial homogeneity $\mathcal{P}$ could differ between biases and variance. In the following, we assume that specific elevation biases, if they exist, are independently corrected and focus on characterizing the elevation variance σ_h^2.

D. Elevation Difference With an Independent Source

After performing affine alignment of elevations $\hat{h}_1(x, y, t_1)$ from a first source $\mathcal{D}_1$ and elevation $\hat{h}_2(x, y, t_2)$ of a second source $\mathcal{D}_2$, we subtract them to derive elevation differences $dh_{1-2}(x, y)$. Assuming independence between the error of each elevation source, the variance of the difference is

$$\sigma^2_{dh_{1-2}}(x, y) = \sigma^2_{h_1}(x, y) + \sigma^2_{h_2}(x, y). \quad (6)$$

By selecting a second source to observe $\hat{h}_2$ that is of higher precision than the first source that observes $\hat{h}_1$, the analysis of the differences $\hat{h}_2 - \hat{h}_1$ will largely capture the variance of the first source. For example, if the second source is three times

more precise than the first, (6) implies that about 95% of the variance of the elevation difference will originate from the first source, yielding

$$\sigma_{h_1}(x,y) \approx \sigma_{dh_{1-2}}(x,y). \tag{7}$$

Alternatively, if h_1 and h_2 originate from independent acquisitions of the same instrument and processing, we have

$$\sigma_{h_1}(x,y) = \frac{\sigma_{dh_{1-2}}(x,y)}{\sqrt{2}}. \tag{8}$$

Thus, we use elevation differences to infer on σ_h, which can be converted from either (7) or (8).

E. Discriminating Elevation Bias From Variance in Spatial Statistics

To further analyze elevation variance, we need to discriminate bias from variance. When analyzing elevation differences, what appears as a bias at the local scale could also be a form of long-range correlation at larger scales [see Fig. 1(b)–(c)]. This distinction is directly related to the assumption of second-order stationarity of spatial statistics. For elevation differences, second-order stationarity implies that the following assumptions should be fulfilled (see Supplementary Section II-A):

1) a first assumption of stationary mean, i.e., that the average of elevation differences $dh(x,y)$ is constant over large areas;
2) a second assumption of stationary variance, i.e., that the variance of elevation differences $\sigma_{dh}(x,y)$ is constant over large areas;
3) a third assumption of spatially consistent covariance, i.e. that the correlation between random errors of elevation differences only depends on the distance between observations.

Large areas here refer to areas slightly smaller than the size of the study domain, typically within an order of magnitude. As such, a correlated error with a correlation range that is orders of magnitude larger than the size of the study domain might be considered a vertical bias common to the entire DEM grid [see Fig. 2]. And, inversely, such a bias placed in the context of a larger study domain might be considered as a correlated error, if the elevation differences fulfill the above assumptions.

Thanks to the affine alignment of our elevation differences, we verify the first assumption of stationary mean. However, the heteroscedasticity of elevations (see Section II-B) invalidates the second and third assumptions, and therefore a nonstationary framework needs to be defined.

F. Nonstationary Spatial Framework for DEM Analysis

To perform spatial statistics with a nonstationary variance, transformation of the data toward a stationary variance is necessary. The transformation depends on the nature of the spatial variability and correlations. In DEMs, we identify two types of correlation: short-range ones related to resolution, and long-range ones related to correlated noise. While the latter appear unrelated to the heteroscedasticity of elevation, the former are similarly linked to local instrument- and terrain-dependent

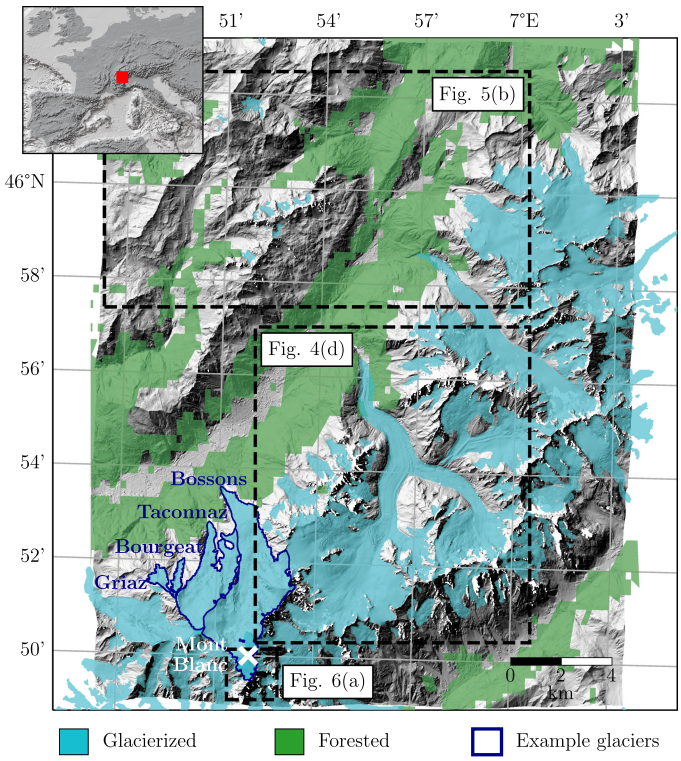

Fig. 3. Mont-Blanc case study. Hillshade of Pléiades DEM and land cover at the Mont-Blanc massif. Example glaciers serve to illustrate Section VI-C.

variables (see Sections II-B–II-C). We thus subdivide elevation variance into elevation heteroscedasticity and spatial correlation of errors [see Fig. 2] assuming that longer-range correlations are independent of elevation heteroscedasticity, which yields

$$\sigma^2_{dh}(x,y) = \sigma^2_{dh_{sr}}(x,y) + \sigma^2_{dh_{lr}} \tag{9}$$

where $\sigma^2_{h_{sr}}(x,y)$ is the variable short-range variance at (x,y), $\sigma^2_{h_{lr}}$ is the constant long-range variance.

Using the variable spread $\sigma_{dh}(x,y)$, the elevation differences can be standardized into a standard score z_{dh} with unit variance, which fulfills the second assumption of second-order stationarity:

$$z_{dh}(x,y) = \frac{dh(x,y)}{\sigma_{dh}(x,y)}. \tag{10}$$

Additionally, the spatial covariance $C_{z_{dh}}$ of z_{dh}, related to the variogram $\gamma_{z_{dh}} = 1 - C_{z_{dh}}$, is also free of the influence of heteroscedasticity and now fulfills the third assumption of second-order stationarity:

$$\gamma^2_{z_{dh}}(d) = \left(\frac{\overline{\sigma_{dh_{sr}}}|_{\mathcal{D}}}{\sigma_{dh}}\right)^2 \gamma_{sr}(d) + \left(\frac{\sigma_{dh_{lr}}}{\sigma_{dh}}\right)^2 \gamma_{lr}(d) \tag{11}$$

where d is the spatial lag, i.e., the distance between two given observations, $\overline{\sigma_{dh_{sr}}}|_{\mathcal{D}}$ is the average of $\sigma_{dh_{sr}}$ in the DEM $\mathcal{D}$, and γ_{sr} and γ_{lr} are the short- and long-range variogram functions.

With all the assumptions in our framework fulfilled, we can now reliably use spatial statistics for uncertainty propagation. To this end, we require an estimate of the elevation dispersion $\sigma_{dh}(x,y)$ and of the variogram of the standard score $\gamma_{z_{dh}}(d)$,

TABLE I
NEARLY SIMULTANEOUS PLÉIADES AND SPOT-6 DEMS USED FOR THE MONT-BLANC CASE STUDY

Instrument	Acquisition time	Resolution of stereo-pair
Pléiades	24/10/2017, 12:00 CET	1.5 m
SPOT-6	25/10/2017, 12:30 CET	0.7 m

which describe the heteroscedasticity and the spatial correlation of errors, respectively. We also need to ensure that our assumption of spatial homogeneity remains valid when using stable terrain as an error proxy to infer heteroscedasticity and spatial correlations on moving terrain. In the following, we address these aspects by utilizing near-simultaneous data and implementing robust methods.

IV. DATA

A. Mont-Blanc Case Study: Simultaneous DEMs

To demonstrate the methods associated with our proposed framework, we present a case study of two DEMs generated one day apart in the Mont-Blanc massif, French Alps [see Fig. 3, Table I]. These DEMs were produced with a spatial posting of 5 m from SPOT-6 and Pléiades stereo images using the Ames Stereo Pipeline [134]. We utilize the temporal closeness of the two acquisitions to assess if stable terrain can be used as a proxy for moving terrain, considering a negligible elevation change on moving terrain.

We present an additional case study in the Northern Patagonian Icefield to illustrate the influence of the quality of stereo-correlation, a sensor-dependent variable, on elevation heteroscedasticity (see Supplementary Section I-A with additional refs. [66], [135], [136]). This case study is based on simultaneously acquired ASTER [47] and SPOT-5 images [see Table S1]. Furthermore, the DEMs used to illustrate noise patterns [see Figs. 1 and S1] are described in the Supplementary Section I-B with additional refs. [137]–[139].

B. Inventory and Land Cover Products

We define moving terrain as glacierized, forested, and seasonally snow-covered terrain, and exclude water bodies from our analysis. The remaining terrain is assumed to be stable. We mask glaciers using the Randolph Glacier Inventory 6.0 (RGI 6.0) outlines [140], which are delineated from images with a typical resolution of 15–30 m. We mask forests and water bodies using the ESA Climate Change Initiative Land Cover version 2.0.7 [141], which has a resolution of 300 m. Forested terrain corresponds to either broadleaved, needleleaved, evergreen, or deciduous tree cover classes.

We identify specific elevation biases over forested terrain between the SPOT-6 and Pléiades DEMs—likely owing to different native resolution, orientation, and spectral bands [see Fig. S3(a)]—and thus exclude this terrain from our analysis. Our end-of-summer acquisitions contain little snow outside of glacierized surfaces. Therefore, we did not mask off-ice snow cover. Ultimately, in our analysis, moving terrain corresponds to glacierized terrain.

V. METHODS

A. Robust Statistics and Alignment

We use the median instead of the mean as a robust estimator of central tendency, and the normalized median absolute deviation (NMAD) instead of the standard deviation as a measure of statistical dispersion. Both choices are to mitigate the effects of frequent outliers in DEMs [142]. Combining these estimators with the dense sampling of stable terrain also ensures robustness to elevation changes of potentially unmasked moving terrain. This includes rare events such as landslides or ground subsidence, or events that can occur over a small portion of the analyzed terrain such as volcanic uplift or sediment transport. We coregister DEMs on stable terrain for horizontal and vertical shifts following the aspect-slope relation described in [77] and we correct for possible tilts through least squares optimization of a plane [71].

B. Heteroscedasticity

We estimate elevation heteroscedasticity by sampling an empirical dispersion of elevation differences $\hat{\sigma}_{dh}$ using the NMAD of binned categories along the terrain slope α [143] and the terrain maximum absolute curvature c [see Figs. 4(a)-(c) and S4]. Maximum absolute curvature is defined as the maximum of the absolute profile curvature and the absolute planform curvature at each location [144]. All terrain attributes are estimated from the Pléiades DEM that contains the least data gaps. When available, the binning can also include an instrument quality factor q, such as the quality of stereo-correlation [see Figs. S5–S7] or interferometric coherence.

We numerically model the empirical dispersion $\hat{\sigma}_{dh}$ as a function σ_{dh} of the terrain- and sensor-dependent variables (α, c, q) by multidimensional linear interpolation of the binned data [see Fig. S8]. The modeling of this variability can also be performed by fitting parametric models, for example, an exponential model with the slope or a linear model with the maximum curvature [see Fig. S9]. These are more robust in the case of small sample sizes of elevation differences.

We standardize the elevation differences dh following (10), using the modeled dispersion $\sigma_{dh}(\alpha, c, q)$:

$$z_{dh} = \frac{dh}{\sigma_{dh}(\alpha, c, q)}. \tag{12}$$

After standardization, we verify that the standard score of the elevation differences matches a normal distribution by quantile-quantile plotting, and by comparison to a normal distribution fit [142], [145] [see Fig. S10]. The substantial improvement validates our choice of terrain slope and maximum curvature as key variables to describe elevation heteroscedasticity, as those largely explain the departure of random elevation errors from normality.

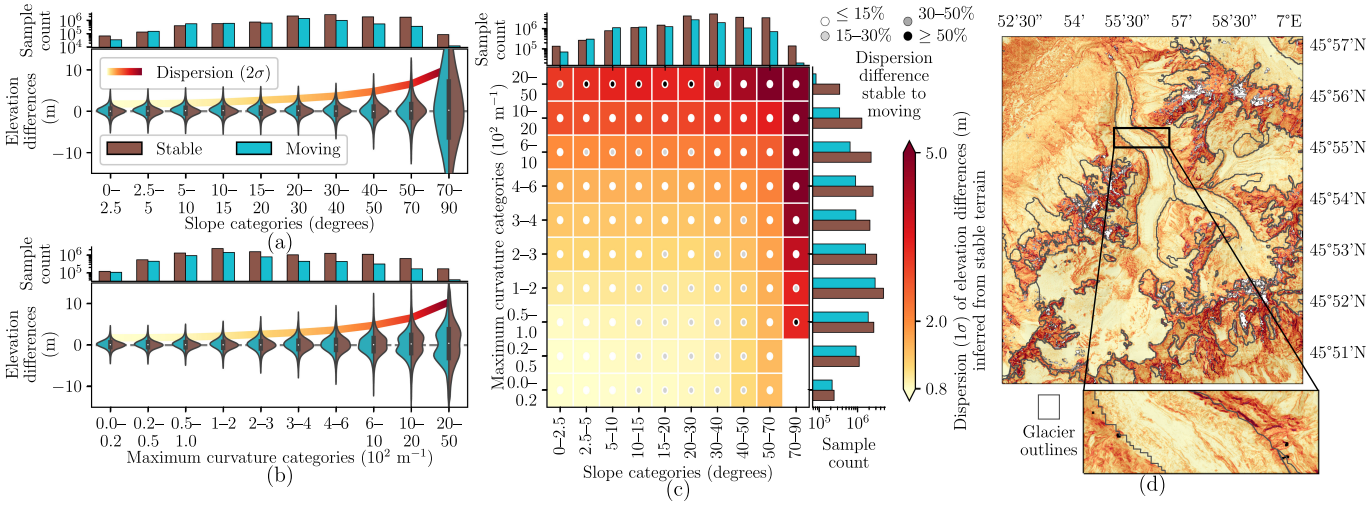

Fig. 4. Heteroscedasticity inference from stable terrain as function of slope and curvature for the Mont-Blanc case study. (a)–(b) Violin plots of elevation differences on stable and moving terrain by bins of (a) slope and (b) maximum curvature. Dispersion inferred from stable terrain is showed by a thick line with color matching other panels. Note the logarithmic scales of histograms. (c) Heatmap of stable terrain dispersion for slope and maximum curvature. Bins with a relative dispersion difference between stable and moving terrain greater than 30% (dark gray and black dots) contain less than 1% of samples. (d) Inferred spatial distribution of vertical precision for all terrain, with inset that matches Fig. 1(a).

C. Spatial Correlations

We estimate spatial correlations by sampling an empirical variogram $\hat{\gamma}$ on the standard score z_{dh} using Dowd's estimator [146], [147] [see Fig. 5(a)]:

$$2\hat{\gamma}_{z_{dh}}(d) = 2.198 \cdot \text{median}(z_{dh}(x,y) - z_{dh}(x',y'))^2 \quad (13)$$

where z_{dh} is the standard score of elevation differences, and locations (x, y) and (x', y') are separated by a spatial lag d.

Dowd's estimator is based on median absolute deviations, and consequently more robust than the Matheron [148] or Cressie–Hawkins [149] estimators classically used (see Supplementary Section II-B based on additional ref. [150]). We verify the increased robustness of Dowd's estimator for the Mont-Blanc case study [see Figs. S11 and S12].

To improve the variogram estimation, we introduce a pairwise subsampling method based on iterative subsetting of pairwise combinations between a disk and multiple rings centered on a random point (see Supplementary Section II-C). As variograms were historically sampled from point measurements [112], traditional sampling methods are less computationally efficient on large grids. Most critically, they are inefficient at sampling pairwise distances evenly across spatial scales, which is substantially improved by our method to estimate more reliably both short-range and long-range correlations [see Fig. S13]. Finally, we derive empirical variograms for 100 independent realizations with the same binning. We estimate our final empirical variogram by the mean of all realizations at each spatial lag with, as an empirical uncertainty, the standard error of the mean.

To derive a spatially continuous representation of the variogram, we calibrate an analytical model γ_{zdh} with the empirical variogram $\hat{\gamma}_{z_{dh}}$. We fit a sum of k variogram models $V(s_k, r_k, d)$, optimizing their partial sills s_k (i.e., correlated variance) and ranges r_k (i.e., correlation length) simultaneously by weighted least squares, using as weights the squared inverse of the empirical uncertainties previously detailed [see Fig. 5(a)]:

$$\gamma_{z_{dh}}(d) = \sum_k V_k(s_k, r_k, d). \quad (14)$$

For the Mont-Blanc study, we find no significant improvement in least-squares residuals when fitting more than three models, which are capable of capturing one short-range and two long-range correlations [see Fig. S14, Table S2]. The two long-range correlations match the along- and cross-track lengths of low-amplitude undulations in the elevation differences [see Fig. 5(b)]. We thus use three models to avoid the possible overfitting of a larger number of summed models. Generally, k should be chosen to reflect the number of distinct ranges in the patterns of DEM noise. For instance, ASTER undulations are characterized by two wavelengths of 1–2 km and 5–10 km in the along-track direction, and a cross-track distance of 60 km [see Fig. S1], which better fits three distinct long-range models [47] for a total of four ranges.

We also identify a low sensitivity to different variogram model types [see Fig. S15, Tables S3, and S4], which shows that adequately modelling the multirange nature of the spatial correlations is more important than refining that of their spatial form [see Fig. 5(b)]. For the Mont-Blanc case study, we reached the smallest least-squares residuals using a gaussian model $G(s, r, x - x')$ at short ranges, and spherical models $S(s, r, x - x')$ at long ranges [151] and used those henceforth:

$$G(s,r,d) = s\left(1 - e^{-\left(\frac{2d}{r}\right)^2}\right), \text{ and} \quad (15)$$

$$S(s,r,d) = \begin{cases} s\left(\frac{3}{2}\frac{d}{r} - \frac{1}{2}\left(\frac{d}{r}\right)^3\right) & \text{if } 0 < d < r \\ s & \text{if } d \geq r. \end{cases} \quad (16)$$

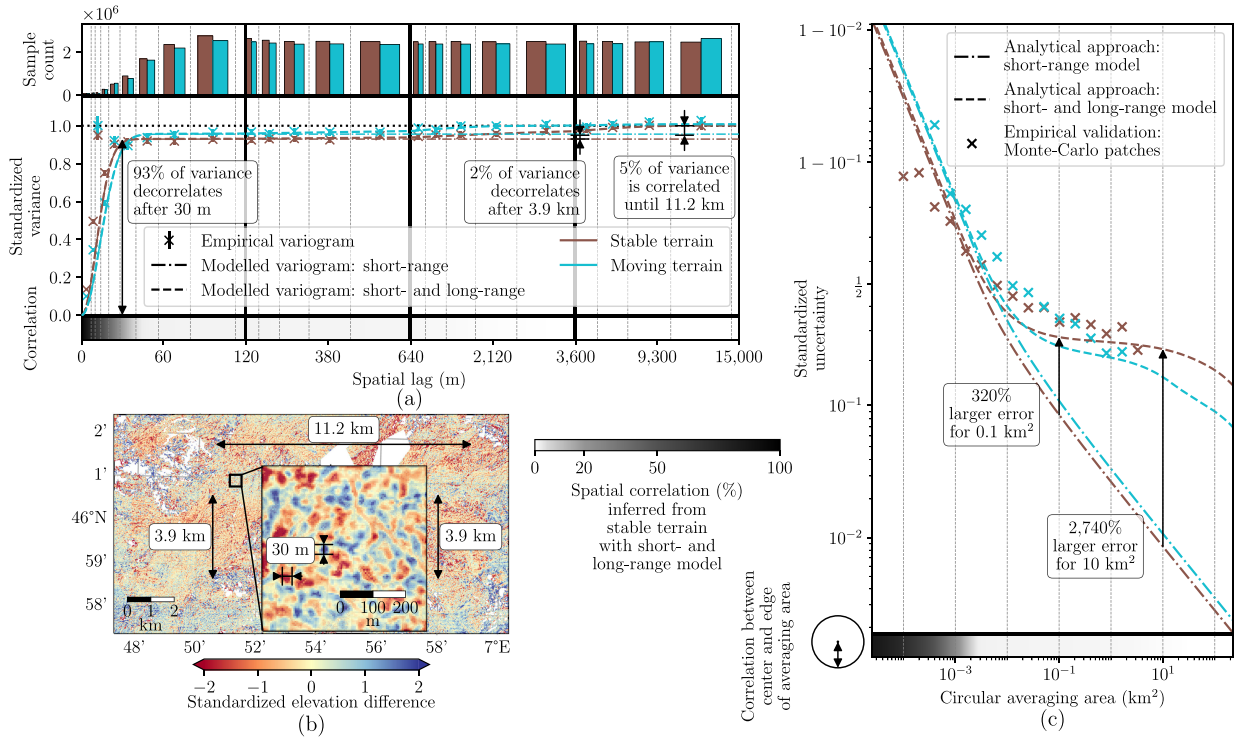

Fig. 5. Spatial correlation inference from stable terrain for the Mont-Blanc case study. (a) Spatial variogram of standardized elevation differences on stable and moving terrain. The empirical variogram is based on Dowd's estimator [146] and modelled by either a short-range spherical model or the sum of short- and long-range spherical models. (b) Excerpt of the standardized elevation difference map, which highlights the correlated signals at both short-range (30 m) and long-range (3.9 km in the along-track direction, 11.2 km in the cross-track direction). (c) Standardized elevation uncertainty with increasing circular averaging area, computed using (18) and validated by empirical Monte Carlo sampling. Note the logit scale of the *Y*-axis.

D. Uncertainty Propagation

1) Simulation Methods for Elevation Derivatives: For derivatives of elevation with a complex spatial gradient, such as terrain slope and aspect later analyzed, we use simulation methods. We find similar results using Fourier randomization [124], [152] and unconditional Gaussian simulation [117], [153], and thus only use the former in the following. For 1,000 realizations, we simulate a random correlated error field of the standard score z_{dh} based on the modeled spatial correlation $\gamma_{z_{dh}}$ in (14). We then de-standardize z_{dh} using (12), and add the resulting elevation error field to the studied DEM. For each of these DEM realizations with an added error field, we then compute the terrain attribute of interest (e.g., terrain slope or aspect), for which we can study the distribution of errors.

2) Theoretical Approximation Methods for Spatial Derivatives: For spatial derivatives such as the average $\overline{dh}$ of elevation changes dh in an area A, we derive an exact analytical solution of the uncertainty in the spatial average $\sigma_{\overline{dh}}$:

$$\sigma^2_{\overline{dh}} = \frac{1}{N^2} \sum_{i=1}^{N} \sum_{j=1}^{N} \rho_{ij} \sigma_{dh_i} \sigma_{dh_j} \tag{17}$$

where N denotes the number of samples i falling in the area A, σ_{dh_i} is the vertical precision of pixel i, and $\rho_{ij} = (1 - \gamma_{z_{dh}}(d))$ is the spatial correlation between pixel i and pixel j based on their distance d.

In practice, (17) raises the issue of scaling exponentially with the number of samples, possibly resulting in trillions of calculations. To remedy this, we propose an approximation for spatially contiguous areas, inspired by the approach of [65] that computes a single aerial integral by approximating the area A by a disk of the same area. Here, for each pixel k of a random subset of K pixels within the N pixels, we compute the single aerial integral of the variogram numerically. We then approximate the variogram integral by the average of these subset aerial integrations (see Supplementary Section II-E):

$$\sigma^2_{\overline{dh}} \approx \overline{\sigma^2_{dh}}|_A \frac{1}{N} \frac{1}{K} \sum_{k=1}^{K} \sum_{i=1}^{N} (1 - \gamma_{z_{dh}}(x_k - x_i)) \tag{18}$$

where $\overline{\sigma^2_{dh}}|_A$ is the average variance of the elevation differences of pixels i in the area A:

$$\overline{\sigma^2_{dh}}|_A = \frac{1}{N} \sum_{i} \sigma^2_{dh_i}. \tag{19}$$

We show that our method improves the accuracy of the theoretical approximation of [65] by accounting for more complex area shapes than disks while maintaining computational efficiency [see Fig. S16]. Additionally, these formulations can be linked to a number of effective samples, which describes the number of samples among the N pixels in area A that are statistically independent based on the spatial correlations modelled by $\gamma_{z_{dh}}$ (see Supplementary Section II-D).

Once uncertainties have been integrated from a spatial support (e.g., pixels) to a larger spatially contiguous ensemble (e.g., glaciers), they can be propagated again to a larger ensemble (e.g., all glaciers in a region) following Krige's relation of transitivity [112], [154]. For this, (17) can be applied for each pair of spatially contiguous ensembles i and j of area A_i with the same variogram $\gamma_{z_{dh}}$ composed of the k summed models $V_k(s_k, r_k, d)$:

$$\sigma_{\overline{dh}} = \frac{1}{(\sum_i A_i)^2} \sum_k \sum_i \sum_j \Big(\sigma_{\overline{dh}_{k,i}} \sigma_{\overline{dh}_{k,j}} - V_k(\sigma_{\overline{dh}_{k,i}} \sigma_{\overline{dh}_{k,j}}, r_k, d_{i-j}) \Big) A_i A_j \tag{20}$$

where d_{i-j} is the distance between the centroids of ensemble i and j, and $\sigma_{\overline{dh}_{k,i}}$ is the spatially integrated uncertainty of ensemble i associated to the variogram model V_k, partial sill s_k and range r_k with pixel pairs n and m:

$$\sigma_{\overline{dh}_{k,i}} = \frac{1}{N^2} \sum_{n=1}^{N} \sum_{m=1}^{N} \left(s_k - V_k(s_k, r_k, x_n - x_m)\right) \sigma_{dh_n} \sigma_{dh_m}. \tag{21}$$

Furthermore, we use a Monte Carlo spatial sampling method to validate our uncertainties of spatially averaged elevations, thus indirectly verifying the robustness of our modeled spatial correlations [see Fig. 5(c)]. We randomly sample up to 10,000 circular patches of area A without replacement. We compute the mean $\overline{dh}$ inside circular patches, keeping only those with more than 80% valid elevation differences dh to mitigate the effects of missing data. We use the NMAD of 10,000 realizations to empirically estimate the uncertainty of the spatially averaged dh of area A, and repeat this procedure for varying area sizes A [see Fig. 5(c)]. This method substitutes repeated correlated simulation of Fourier randomization or Gaussian simulation by a repeated spatial sampling, relying on the assumption of spatial homogeneity of variance on stable terrain (see Section III-C). As it requires a large number of independent patches to produce a robust estimate, the area size A for which it can estimate an uncertainty is limited to sizes much smaller than that of the spatial domain. It is also highly dependent on the availability of stable terrain. Therefore, we use it only for validation purposes.

VI. Results and Discussion

In Section VI-A below, we discuss the use of stable terrain as an error proxy based on the methods applied to the Mont-Blanc case study. In Sections VI-B and VI-C, we then analyze the impacts of heteroscedasticity and spatial correlations when propagating elevation variance into uncertainties of pixel-scale elevation derivatives such as terrain slope, or spatial derivatives such as glacier volume changes. In those two sections, we provide examples based on the Mont-Blanc case study and determine the impact of our methods for a set of assumptions on the variance properties during uncertainty propagation:

1) either homoscedastic elevation (constant variance, shortened "homosc") or heteroscedastic elevation (variable variance, "heterosc"); and
2) either no spatial correlation (shortened "no corr."), or only short-range correlations ("short-range"), or both short- and long-range correlations ("long-range").

In this exercise, the most realistic case refers to the one that accounts for potential elevation heteroscedasticity and potential short- and long-range correlations. Uncertainties are reported as a symmetric confidence interval of 1σ (68% confidence level) or 2σ (95%), specified in each case.

TABLE II
Estimated Variogram Model Parameters for the Spatial Correlations of Elevation Errors in the Mont-Blanc Case Study

Model parameters	Stable	Moving
Sill of short-range model	93%	95%
Range of short-range model	30 m	38 m
Sill of 1st long-range model	2%	4%
Range of 1st long-range model	3,900 m	2,400 m
Sill of 2nd long-range model	5%	1%
Range of 2nd long-range model	11,200 m	10,800 m

Note: Stable and moving terrain is distinguished (columns). Gaussian components are listed for the short-range model and spherical components for the long-range ones, as in Fig. 5. Partial sills are expressed as a percentage of the total variance.

A. Validation of Stable Terrain as an Error Proxy

We test the validity of using stable terrain as a proxy of elevation errors for moving terrain on the nearly simultaneous DEMs of the Mont-Blanc case study. We find that elevations on moving terrain exhibit the same heteroscedasticity with slope and curvature than those on stable terrain, with less than 1% of binned samples that differ by more than 30% [see Fig. 4(a)–(c)]. We additionally verify that this elevation heteroscedasticity is continuous between neighboring bins when using robust estimators, thereby consolidating our assumption of spatial homogeneity (see Section III-C). By extending this assumption to the case of moving terrain, we infer a complete map of vertical precision [see Fig. 4(d)].

We find similar spatial correlations of errors between stable and moving terrain [see Fig. 5(a)]. Values of partial sills and ranges of the variogram models that describe these correlations are within the same orders of magnitude [see Table II], despite greater differences at long ranges due to the limited pairwise samples available on moving terrain. Using our Monte Carlo sampling method, we validate the increased robustness of using multiple correlation ranges to estimate uncertainties across spatial scales [see Fig. 5(c)]. Our results indicate that using a short-range model alone underestimates elevation uncertainties by several orders of magnitude for areas larger than 0.1 km^2.

For elevation heteroscedasticity, our results highlight the importance of elevation standardization to ensure an adequate scaling when inferring on another type of terrain (e.g., from steep, stable terrain to flat, moving terrain). Yet, our analysis only exemplifies snow- and ice-covered terrain with high-resolution stereophotogrammetric DEMs. The physical properties of the observed terrain in relation to the utilized sensor might in some

cases invalidate our assumption of spatial homogeneity. For instance, we found that our standardization did not mitigate the larger errors of elevation over forested areas [see Fig. S3(a)]. In such a case, an upfront investigation of specific elevation biases is required. After these biases are corrected, a refined modeling of elevation heteroscedasticity based on sensor-dependent variables can help to reach a good description of the properties of spatial homogeneity. We indeed found a strong relationship with the quality of stereo-correlation for the case study of the Northern Patagonian Icefield [see Figs. S6 and S7]. The rougher resolution (15 m) and spectral range (8 bits) of the ASTER stereo images, compared to those of SPOT-6 and Pléiades (metric resolution and 12-bits), leads to a significant variability in elevation errors with terrain texture.

For spatial correlations, we highlight the value of standardization to reduce variability for empirical variogram estimation [see Figs. S3 and S12]. It is especially useful to deconvolve the long-range correlations with small magnitude to the short-range ones. Heteroscedasticity may indeed explain the short-range variogram anisotropy found by previous studies [155]. We nevertheless identify a slight difference in the well-constrained short correlation range between stable and moving terrain (30 m vs. 38 m, respectively; Table II). This difference might be due to the rougher interpolation of stereophotogrammetric block-matching algorithms over bright, lower-texture glacierized terrain. In some cases, sensor properties or processing schemes influence not only the magnitude of spatial variability but also the scale of correlations. Developing a statistical framework that continuously includes these effects might be overly complex for most analyses that, instead, could adjust estimates of short-range correlation depending on the type of observed terrain.

We conclude that stable terrain is a valid proxy for error analysis, provided that elevation heteroscedasticity is taken into account. However, the quality of statistical inference from this error proxy depends directly on the number of stable terrain samples available. For some DEMs, these samples might be scarce in the proximity of continuous expanses of moving terrain (e.g., at the margins of ice sheets or large forests) and thus insufficient to perform robust inference. To address this, the stable terrain of independent DEMs, possibly located elsewhere, could be utilized if they are generated from the same instrument and processing chain. Many DEMs indeed have consistent error properties between segments acquired under similar conditions around the world (e.g., [47], [59], [156]). For instruments with correlated noise of varying amplitude, such as Pléiades or ASTER, long-range correlations can be more robustly inferred from a multiple-acquisition average of variograms.

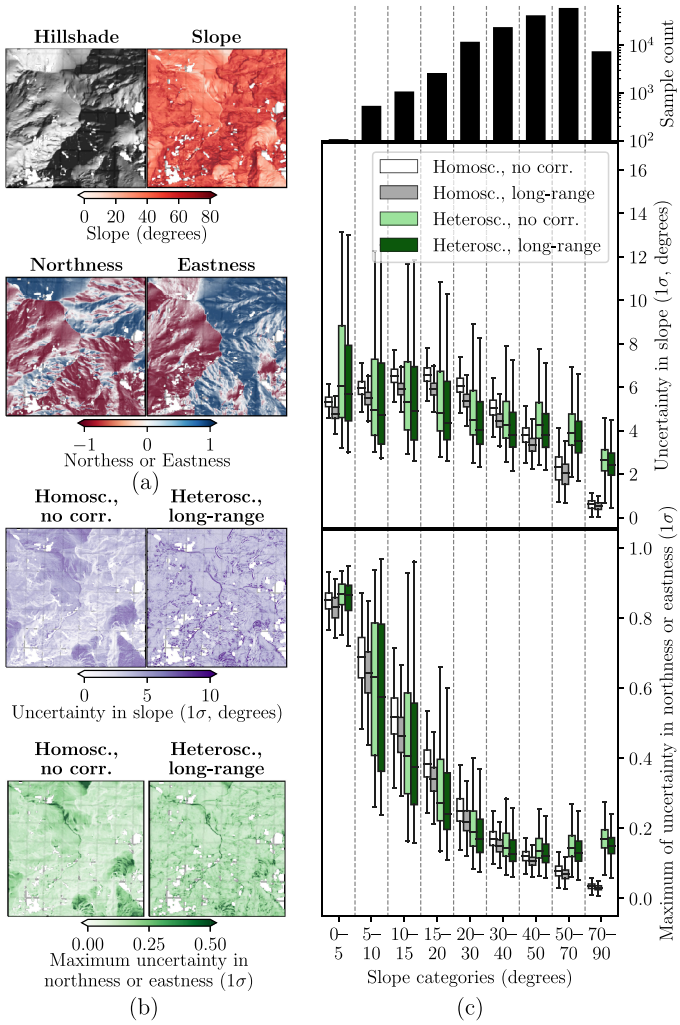

Fig. 6. Uncertainty propagation to terrain slope and aspect at the Mont-Blanc summit. (a) Hillshade and terrain attributes based on the Pléiades DEM for a 4 km^2 area centered on Mont Blanc. (b) Slope and aspect uncertainty estimated by the half-difference between the 16th and 84th percentiles of 1,000 simulated terrain attributes at each pixel. (c) Distributions of slope and aspect uncertainties by category of terrain slope for each set of assumptions, with boxes denoting the interquartile range and whiskers extending to the entire distribution.

B. Impact on Pixel-Scale Derivatives of Elevation: Example With Terrain Slope and Aspect

We illustrate the propagation of elevation uncertainty to the terrain slope and aspect in a 4 km^2 area around the Mont-Blanc summit [see Fig. 6(a)]. We select this area due to its wide range of slopes and aspects, and its small extent facilitating computationally expensive simulations. To avoid the circularity of the aspect variable when assessing uncertainty, we divide it into northness (i.e., cosine of the aspect) and eastness (i.e., sine of the aspect) which denote, respectively, the north–south and east–west tilt of the slope.

We propagate uncertainties in the Pléiades DEM by simulating random elevation error fields (see Section V-D) for every set of assumptions [see Fig. S17]. For this example, we assume that SPOT-6 and Pléiades have random errors of similar amplitude, and estimate the random errors of the Pléiades DEM following (8). We generally note a strong deviation from normality and asymmetry in the simulated uncertainty distribution of terrain attributes [see Fig. S18]. While this asymmetry requires specific considerations for in-depth terrain analysis, we here provide a simplified picture by estimating a symmetric 1σ uncertainty derived from the half-difference between the 16th and 84th percentile of the simulated slope, northness or eastness of each pixel.

Our analysis reveals that elevation heteroscedasticity plays a major role in the spatial distribution of uncertainties in slope and aspect. In particular, it exacerbates errors in steep and rough terrain. Spatial correlations moderately affect uncertainties by slightly reducing their amplitude [see Fig. 6(b)–(c)]. We interpret the latter to be due to an increase in the spatial coherence of terrain derivatives when the elevation errors are spatially correlated. Since topographical attributes are derived over a 3 $\times$ 3 pixel window, the closer the short-range spatial correlations are to a 3-pixel length, the larger the impact on the amplitude change [see Fig. S19].

By aggregating uncertainties into slope categories, we show that uncertainties in flat terrain are overestimated when assuming homoscedasticity and no spatial correlation, while those in steep terrain are underestimated by up to a factor of 10 [see Fig. 6(c)]. Slope uncertainties decrease near slopes of 90 degrees, likely because elevation errors tilt the terrain in different orientations while generally maintaining a steep slope, which translates into aspect uncertainties. We reach similar conclusions when aggregating uncertainties by maximum absolute curvature categories, our second variable that describes elevation heteroscedasticity [see Fig. S20].

C. Impact on Spatial Derivatives of Elevation: Example With Glacier Volume Changes

We consider 84 glaciers in the Mont-Blanc massif that have at least 85% of their area covered by valid elevation differences. We analyze the mean elevation changes within the outline of each glacier, which can be converted to volume changes after multiplication by the glacier area, and propagate uncertainties for each set of assumptions.

We find that spatial correlations strongly hamper the decrease in uncertainty with increasing glacier area [see Fig. 7(a)]. Long-range correlations are the main contributor to uncertainty for large areas, mirroring the validation of Fig. 5(c). While long-range correlations account for only 7% of the variance in our case study, uncertainties of mean elevation changes for glaciers larger than 10 km^2 are underestimated by a factor of about 25 when based solely on short-range correlation. This is striking, and even more so when realizing that the underestimation is nearly by a factor of 150 when totally omitting spatial correlations. This dramatic increase is explained by the fact that long-range correlations essentially correspond to local biases.

Heteroscedasticity has a moderate influence on the uncertainty of each glacier, impacting its amplitude by a factor of 1 to 3. The uncertainty of glaciers located in flat areas is overestimated when using a homoscedastic assumption due to the larger average variance over rougher, stable terrain. On the contrary, the uncertainty of the steepest glaciers is underestimated [see Fig. 7(b)]. Using the empirical comparison provided by the nearly simultaneous volume changes, we show that the uncertainties for the mean elevation change are most realistic when accounting for long-range spatial correlation [see Fig. 7(c)]. In such a case, 89% of the ranges intersect zero (the true volume change) at the 2σ level (i.e., 95% confidence), in contrast to

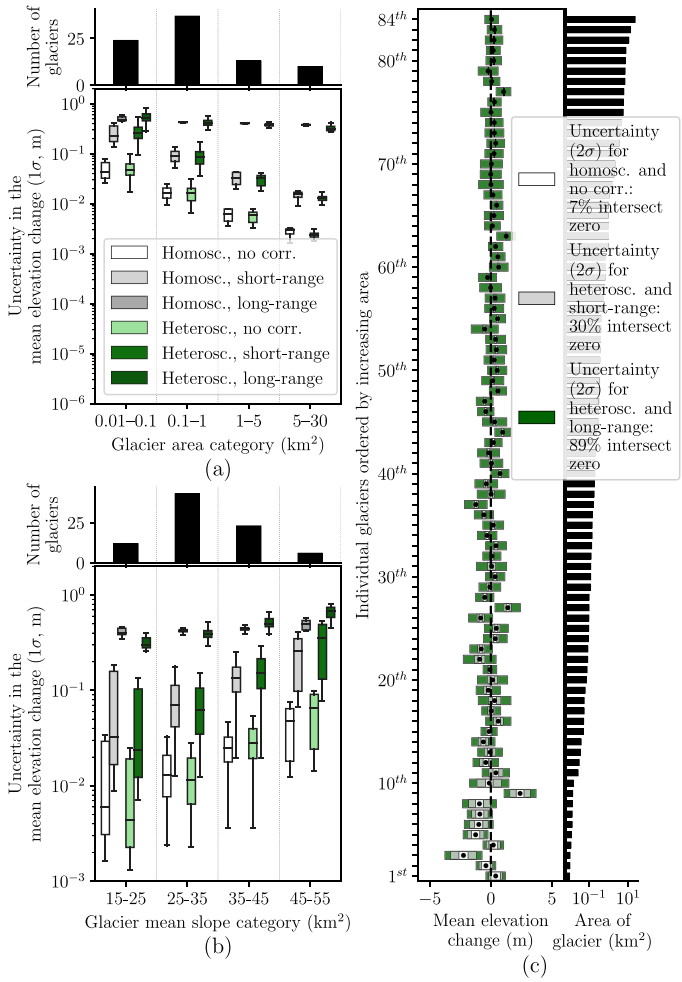

Fig. 7. Uncertainty propagation to glacier mean elevation changes at the Mont-Blanc massif. (a)–(b) Distributions of uncertainty of glacier mean elevation change by category of area and average terrain slope for each set of assumption, with boxes denoting the interquartile range and whiskers extending to the entire distribution. (c) Empirical evaluation of uncertainty ranges for mean glacier elevation changes in the Mont-Blanc case study. Correct uncertainty estimates should cross the vertical zero line in 95% of the cases.

only 30% for short ranges and 7% for no correlation. Yet, our uncertainties are slightly too low.

We identify the cause of this underestimation as the omission of a longer-range correlation close to the size of the DEM and thereby difficult to constrain. This longer-range correlation arises from the fact that along-track undulations are fully correlated in the 20-km-wide cross-track direction. Directional variography could help characterize such correlations, but would lead to a more difficult uncertainty propagation, with exacerbated complexity when combining several DEMs. Instead, we maintain an omnidirectional variogram to describe correlations, but assess a conservative estimate based on artificial undulations [see Fig. S21]. This results in the replacement of the 11.2-km correlation with a 20-km one (swath width) and a partial sill twice larger. We then find that 93% of the uncertainties for glacier larger than 0.2 km^2 intersect zero at the 95% confidence level, confirming the increased robustness with these considerations. Only 87% do so for smaller

TABLE III
SPATIAL UNCERTAINTY PROPAGATION AMONG GLACIERS IN THE MONT-BLANC MASSIF

Uncertainty of spatial average	Griaz and Bourgeat	Bossons and Taconnaz	All glaciers
$\sigma_{\overline{dh}}$ no corr. (m)	0.027	0.006	0.002
$\sigma_{\overline{dh}}$ short-range corr. (m)	0.027	0.006	0.002
$\sigma_{\overline{dh}}$ long-range corr. (m)	0.061	0.049	0.024
Glacier area (km^2)	0.9	16.3	131.1

Mean elevation change uncertainties $\sigma_{\overline{dh}}$ are propagated using (20).

glaciers, however. This discrepancy might be explained by unaccounted heteroscedasticity from landform-projected shadows that particularly affects small glaciers in steep and north-facing slopes.

When uncertainties of volume change of several glaciers are propagated into that of the massif, correlations also come into play. We illustrate the propagation at different spatial scales by considering several glacier groups: one group with the two small neighboring glaciers of Griaz and Bourgeat, another group with the two large neighboring glaciers of Bossons and Taconnaz, and a third group including all 84 glaciers [see Fig. 3]. We find identical uncertainties when considering no correlation, or only short-range correlations [see Table III]. This reflects the fact that all glaciers are separated by at least 30 m, i.e. a distance larger than that of our short-range correlation [see Table II]. Long-range spatial correlations have a large impact on the total uncertainty, however, with a tenfold underestimation of the uncertainty for all glaciers in the massif when omitting them. Increased uncertainties from long-range correlations mostly affect large neighboring glaciers, as shown for Bossons and Taconnaz, but also affect smaller, disconnected glaciers such as Griaz and Bourgeat. The latter is true as long as the glaciers are within the correlation range of 11.2 km.

VII. CONCLUSION

In this study, we reviewed the literature on the accuracy and precision of DEMs. On the basis of the raised considerations regarding variable vertical precision and correlated noises, we proposed a nonstationary spatial framework for DEM uncertainty analysis. This framework allows to perform inference on a single difference between a DEM and independent elevation data on stable terrain, and to distinguish elevation biases from elevation variance. We developed robust methods to estimate and model both elevation heteroscedasticity and spatial correlation of elevation errors. We then validated that stable terrain is a reliable error proxy for other terrain types using pairs of DEMs derived from nearly simultaneous acquisitions for the Mont-Blanc massif and the Northern Patagonian Icefield.

We illustrated the impact of our methods when propagating uncertainties to pixel-scale and spatial derivatives of elevation. For the pixel-scale terrain slope, uncertainties are underestimated by up to a factor 10 in rough and steep topography when omitting elevation heteroscedasticity. For glacier volume changes, the uncertainty of the volume change of a glacier of 10 km^2 is underestimated by a factor of 25 when omitting correlations with ranges of 3.9 and 11.2 km, despite their small cumulative magnitude of only 7% of the variance. This underestimation of long-range spatial correlation affects many studies relying on instruments plagued by noise, such as the widely used DEMs from SRTM and ASTER.

We provide an implementation of our methods in the Python package xDEM [157], which includes, in particular, DEM alignment, correction, and uncertainty analysis. Spatial statistics have long been used for uncertainty analysis, yet often suffered from a lack of accessibility [126]. The wider application of such analysis was still deemed as "unrealized" a decade ago [133], possibly also due to the scarcity of open-source and documented tools for spatial statistics. By providing our methodological tools within the frame of a package embedded in high-level programming languages that efficiently pairs with remote sensing analysis, we hope to foster a consistent, reproducible and accessible uncertainty analysis of DEMs.

We highlight the genericity of our spatial framework for uncertainty analysis and of our estimation methods for dense and outlier-prone grid data. Our framework holds the potential to be extended to other geospatial data. Gridded surface displacements, for instance, profit from the same error proxy of stable terrain and are increasingly used in a variety of applications. To describe the precision of such spatially structured data, we advocate for the use of additional metrics. These metrics should describe potential heteroscedasticity and spatial correlation of errors, reported, for example, in a tabular manner—parameters of variogram models; discrete categories of heteroscedasticity. Ultimately, the adoption of such new metrics is critical to progress towards a realistic description of error structure in geospatial data, and a robust propagation of uncertainties in Earth observation science.

DATA AND CODE AVAILABILITY STATEMENT

The code developed for the processing and analysis of all data, and the generation of figures and tables in this article is available at https://github.com/rhugonnet/dem_error_study, with routines implemented in the DEM analysis Python package xDEM available at https://github.com/GlacioHack/xdem with supporting documentation at https://xdem.readthedocs.io, and the spatial statistics Python package SciKit-GStat available at https://github.com/mmaelicke/scikit-gstat with supporting documentation at https://scikit-gstat.readthedocs.io.

AUTHOR CONTRIBUTIONS

R.H., F.B. and E.B. designed the study. F.B. performed an early analysis of spatial correlation for the Mont-Blanc case study. R.H. developed and tested nonstationary spatial statistics methods for DEMs with inputs from N.E., A.D., F.B. and E.B. R.H. implemented the methods in the Python package xDEM with main inputs from A.D. and E.M. All authors interpreted the results. R.H. performed the literature review and led the writing of the paper, and all other co-authors contributed.

ACKNOWLEDGMENT

The authors would like to thank Dorde Masovic for realizing Fig. 2 with vector graphics. The authors would also like to thank Alexandre Wadoux for insightful exchanges on spatial statistics, Simon Gascoin for discussions on along-track undulations in Pléiades DEMs, and Eyjólfur Magnússon and Joaquín Belart for providing insights into Gaussian simulations for DEMs. The authors finally thank Jonathan Bamber, César Deschamps-Berger and Matthias Huss for comments on early versions of the manuscript. SPOT6/7 data were obtained from GEOSUD (ANR-10-EQPX-20, programme 'Investissements d'Avenir'). INRAE is a member of Labex OSUG. R.H. acknowledges a fellowship from the University of Toulouse. R.H., A.D., E.M and D.F. acknowledge funding from the Swiss National Science Foundation, Grant 184634. E.B. acknowledges support from the French Space Agency (CNES) through ISIS and TOSCA programmes.

REFERENCES

[1] H. Taud, J.-F. Parrot, and R. Alvarez, "DEM generation by contour line dilation," *Comput. Geosci*., vol. 25, no. 7, pp. 775–783, Aug. 1999.

[2] Q. Weng, "Quantifying uncertainty of digital elevation models derived from topographic maps," in *Proc. Adv. Spatial Data Handling*. Berlin Germany: Springer, 2002, pp. 403–418.

[3] P. A. Rosen et al., "Synthetic aperture radar interferometry," *Proc. IEEE*, vol. 88, no. 3, pp. 333–382, Mar. 2000.

[4] R. Bürgmann, P. A. Rosen, and E. J. Fielding, "Synthetic aperture radar interferometry to measure earth's surface topography and its deformation," *Annu. Rev. Earth Planet. Sci*., vol. 28, no. 1, pp. 169–209, May 2000.

[5] A. S. Walker, "Analogue, analytical and digital photogrammetric workstations: Practical investigations of peformance," *Photogrammetric Rec.*, vol. 15. no. 85, pp. 17–25, 1995.

[6] E. M. Mikhail, J. S. Bethel, and J. C. McGlone, *Introduction to Modern Photogrammetry*. Hoboken, New Jersey, USA: John Wiley & Sons, Mar. 2001, vol. 19.

[7] E. P. Baltsavias, "Airborne laser scanning: Basic relations and formulas," *ISPRS J. Photogramm. Remote Sens*., vol. 54, no. 2/3, pp. 199–214, Jul. 1999.

[8] R. O. Dubayah and J. B. Drake, "Lidar remote sensing for forestry," *J. For*., vol. 98, no. 6, pp. 44–46, Jun. 2000.

[9] S. Bhushan, D. Shean, O. Alexandrov, and S. Henderson, "Automated digital elevation model (DEM) generation from very-high-resolution planet SkySat triplet stereo and video imagery," *ISPRS J. Photogramm. Remote Sens*., vol. 173, pp. 151–165, Mar. 2021.

[10] J. Biggs and T. J. Wright, "How satellite InSAR has grown from opportunistic science to routine monitoring over the last decade," *Nat. Commun*., vol. 11, no. 1, Aug. 2020, Art. no. 3863.

[11] J. Rosen, "Shifting ground," *Science*, vol. 371, no. 6532, pp. 876–880, Feb. 2021.

[12] N. Galiatsatos, D. N. M. Donoghue, and G. Philip, "High resolution elevation data derived from stereoscopic CORONA imagery with minimal ground control," *Photogrammetric Eng. Remote Sens.*, vol. 73, no. 9, pp. 1093–1106, 2007.

[13] A. Dehecq et al., "Automated processing of declassified KH-9 hexagon satellite images for global elevation change analysis since the 1970s," *Front Earth Sci*., vol. 8, 2020, Art. no. 516.

[14] E. C. Geyman, W. J. J. van Pelt, A. C. Maloof, H. F. Aas, and J. Kohler, "Historical glacier change on svalbard predicts doubling of mass loss by 2100," *Nature*, vol. 601, no. 7893, pp. 374–379, Jan. 2022.

[15] G. LeFavour and D. Alsdorf, "Water slope and discharge in the amazon river estimated using the shuttle radar topography mission digital elevation model," *Geophys. Res. Lett*., vol. 32, no. 17, Sep. 2005, Art. no. L17404.

[16] J. Oksanen and T. Sarjakoski, "Error propagation analysis of DEM-based drainage basin delineation," *Int. J. Remote Sens*., vol. 26, no. 14, pp. 3085–3102, Jul. 2005.

[17] L. Hawker, P. Bates, J. Neal, and J. Rougier, "Perspectives on digital elevation model (DEM) simulation for flood modeling in the absence of a High-Accuracy open access global DEM," *Front Earth Sci*., vol. 6, 2018, Art. no. 233.

[18] B. Székely and D. Karátson, "DEM-based morphometry as a tool for reconstructing primary volcanic landforms: Examples from the Börzsöny mountains, hungary," *Geomorphology*, vol. 63, no. 1, pp. 25–37, Nov. 2004.

[19] T. Bolch, U. Kamp, J. Olsenholler, and M. Oluić, "Using ASTER and SRTM DEMs for studying geomorphology and glaciation in high mountain areas," in *New Strategies for European Remote Sensing*, M. Oluić, Ed. Rotterdam: Millpress, 2005, pp. 119–127.

[20] B. Žabota, B. Repe, and M. Kobal, "Influence of digital elevation model resolution on rockfall modelling," *Geomorphology*, vol. 328, pp. 183–195, Mar. 2019.

[21] A. Mueting, B. Bookhagen, and M. R. Strecker, "Identification of debris-flow channels using high-resolution topographic data: A. case study in the quebrada del toro, NW argentina," *J. Geophys. Res. Earth Surf*., vol. 126, no. 12, Dec. 2021, Art. no. e2021JF006330. [Online]. Available: https://doi.org/10.1029/2021JF006330

[22] A. Ganas, G. Papadopoulos, and S. B. Pavlides, "The 7 september 1999 athens 5.9 ms earthquake: Remote sensing and digital elevation model inputs towards identifying the seismic fault," *Int. J. Remote Sens*., vol. 22, no. 1, pp. 191–196, Jan. 2001.

[23] S. Vassilopoulou et al., "Orthophoto generation using IKONOS imagery and high-resolution DEM: A case study on volcanic hazard monitoring of nisyros island (Greece)," *ISPRS J. Photogramm. Remote Sens*., vol. 57, no. 1, pp. 24–38, Nov. 2002.

[24] P. Grosse, B. van Wyk de Vries, P. A. Euillades, M. Kervyn, and I. A. Petrinovic, "Systematic morphometric characterization of volcanic edifices using digital elevation models," *Geomorphology*, vol. 136, no. 1, pp. 114–131, Jan. 2012.

[25] K. K. Singh and A. Singh, "Detection of 2011 sikkim earthquake-induced landslides using neuro-fuzzy classifier and digital elevation model," *Nat. Hazards*, vol. 83, no. 2, pp. 1027–1044, Sep. 2016.

[26] Y. Bühler, S. Kumar, J. Veitinger, M. Christen, A. Stoffel, and Others, "Automated identification of potential snow avalanche release areas based on digital elevation models," *Nat. Hazards Earth Syst. Sci*., vol. 13, no. 5, pp. 1321–1335, 2013.

[27] A. E. Akay, H. Oğuz, I. R. Karas, and K. Aruga, "Using LiDAR technology in forestry activities," *Environ. Monit. Assess*., vol. 151, no. 1–4, pp. 117–125, Apr. 2009.

[28] A. Räsänen, M. Kuitunen, E. Tomppo, and A. Lensu, "Coupling high-resolution satellite imagery with ALS-based canopy height model and digital elevation model in object-based boreal forest habitat type classification," *ISPRS J. Photogramm. Remote Sens*., vol. 94, pp. 169–182, Aug. 2014.

[29] J. Griffin et al., "An evaluation of onshore digital elevation models for modeling tsunami inundation zones," *Front Earth Sci*., vol. 3, 2015, Art. no. 32.

[30] S. Kulp and B. H. Strauss, "Global DEM errors underpredict coastal vulnerability to sea level rise and flooding," *Front Earth Sci*., vol. 4, 2016, Art. no. 36.

[31] A. Hooijer and R. Vernimmen, "Global LiDAR land elevation data reveal greatest sea-level rise vulnerability in the tropics," *Nat. Commun*., vol. 12, no. 1, Jun. 2021, Art. no. 3592.

[32] M. K. Barker, E. Mazarico, G. A. Neumann, M. T. Zuber, J. Haruyama, and D. E. Smith, "A new lunar digital elevation model from the lunar orbiter laser altimeter and SELENE terrain camera," *Icarus*, vol. 273, pp. 346–355, Jul. 2016.

[33] Y. Wang and B. Wu, "Active machine learning approach for crater detection from planetary imagery and digital elevation models," *IEEE Trans. Geosci. Remote Sens*., vol. 57, no. 8, pp. 5777–5789, Aug. 2019.

[34] Y.-C. Hsieh, Y.-C. Chan, and J.-C. Hu, "Digital elevation model differencing and error estimation from multiple sources: A case study from the meiyuan shan landslide in taiwan," *Remote Sens.*, vol. 8, no. 3, Feb. 2016, Art. no. 199.

[35] P. Lacroix, "Landslides triggered by the gorkha earthquake in the langtang valley, volumes and initiation processes the 2015 gorkha, Nepal, earthquake and himalayan studies: First results 4. seismology," *Earth Planets Space*, vol. 68, no. 1, pp. 1–10, 2016.

[36] D. H. Shugar et al., "A massive rock and ice avalanche caused the 2021 disaster at chamoli, indian himalaya," *Science*, vol. 373, no. 6552, pp. 300–306, Jun. 2021.
[37] M. Nolan, C. Larsen, and M. Sturm, "Mapping snow depth from manned aircraft on landscape scales at centimeter resolution using structure-from-motion photogrammetry," *Cryosphere*, vol. 9, no. 4, pp. 1445–1463, Aug. 2015.
[38] R. Marti, S. Gascoin, E. Berthier, M. d. Pinel, T. Houet, and D. Laffly, "Mapping snow depth in open alpine terrain from stereo satellite imagery," *Cryosphere*, vol. 10, no. 4, pp. 1361–1380, 2016.
[39] C. Deschamps-Berger et al., "Snow depth mapping from stereo satellite imagery in mountainous terrain: Evaluation using airborne laser-scanning data," *Cryosphere*, vol. 14, no. 9, pp. 2925–2940, Sep. 2020.
[40] M. Bagnardi, P. J. González, and A. Hooper, "High-resolution digital elevation model from tri-stereo pleiades-1 satellite imagery for lava flow volume estimates at fogo volcano," *Geophys. Res. Lett*., vol. 43, no. 12, pp. 6267–6275, Jun. 2016.
[41] G. B. M. Pedersen et al., "Hekla volcano, iceland, in the 20th century: Lava volumes, production rates, and effusion rates," *Geophys. Res. Lett*., vol. 45, no. 4, pp. 1805–1813, Feb. 2018.
[42] C. Ticehurst, S. Phinn, and A. Held, "Using multitemporal digital elevation model data for detecting canopy gaps in tropical forests due to cyclone damage: An initial assessment," *Austral Ecol*., vol. 32, no. 1, pp. 59–69, Feb. 2007.
[43] L. Magruder, H. Leigh, and A. Neuenschwander, "Evaluation of terrain and canopy height products in central african tropical forests," *Int. J. Remote Sens*., vol. 37, no. 22, pp. 5365–5387, Nov. 2016.
[44] K. Gdulová, J. Marešová, V. Barták, M. Szostak, J. Červenka, and V. Moudrý, "Use of TanDEM-X and SRTM-C data for detection of deforestation caused by bark beetle in central european mountains," *Remote Sens.*, vol. 13, no. 15, Aug. 2021, Art. no. 3042.
[45] D. Felikson et al., "Inland thinning on the greenland ice sheet controlled by outlet glacier geometry," *Nat. Geosci*., vol. 10, no. 5, pp. 366–369, May 2017.
[46] D. E. Shean, I. R. Joughin, P. Dutrieux, B. E. Smith, and E. Berthier, "Ice shelf basal melt rates from a high-resolution digital elevation model (DEM) record for pine island glacier, antarctica," *Cryosphere*, vol. 13, no. 10, pp. 2633–2656, 2019.
[47] R. Hugonnet et al., "Accelerated global glacier mass loss in the early twenty-first century," *Nature*, vol. 592, no. 7856, pp. 726–731, Apr. 2021.
[48] J. Wood, "The geomorphological characterisation of digital elevation models," Ph.D. dissertation, University of Leicester (U.K.), Ann Arbor, USA, 1996.
[49] B. H. Carlisle, "Digital elevation model quality and uncertainty in DEM-based spatial modelling," Ph.D. dissertation, University of Greenwich, London, U.K., 2002.
[50] J. Oksanen, "Digital elevation model error in terrain analysis," Ph.D. dissertation, University of Helsinki, Faculty of Science, Helsinki, Finland, Nov. 2006.
[51] C. Papasaika-Hanusch, "Fusion of digital elevation models," Ph.D. dissertation, ETH Zurich, Zurich, Switzerland, 2012.
[52] D. F. Maune, *Digital Elevation Model Technologies and Applications: The DEM Users Manual*, Bethesda, Maryland, American Society for Photogrammetry and Remote Sensing, 2007.
[53] P. F. Fisher and N. J. Tate, "Causes and consequences of error in digital elevation models," *Prog. Phys. Geography: Earth Environ.*, vol. 30, no. 4, pp. 467–489, Aug. 2006.
[54] S. P. Wechsler, "Uncertainties associated with digital elevation models for hydrologic applications: A review," *Hydrol. Earth Syst. Sci*., vol. 11, no. 4, pp. 1481–1500, Aug. 2007.
[55] S. E. Lakshmi and K. Yarrakula, "Review and critical analysis on digital elevation models," *Geofizika*, Andrija MohoroviČiĆ Geophysical Institute, Department of Geophysics, Faculty of Science, University of Zagreb, Croatia, vol. 35, no. 2, pp. 129–157, 2018.
[56] L. Polidori and M. El Hage, "Digital elevation model quality assessment methods: A. critical review," *Remote Sens.*, vol. 12, no. 21, Oct. 2020, Art. no. 3522.
[57] F. Hebeler and R. S. Purves, "The influence of elevation uncertainty on derivation of topographic indices," *Geomorphology*, vol. 111, no. 1, pp. 4–16, Oct. 2009.
[58] T. G. Farr et al., "The shuttle radar topography mission," *Rev. Geophys*., vol. 45, no. 2, May 2007, Art. no. 1485.
[59] P. Rizzoli et al., "Generation and performance assessment of the global TanDEM-X digital elevation model," *ISPRS J. Photogramm. Remote Sens*., vol. 132, pp. 119–139, 2017.
[60] G. Amatulli, D. McInerney, T. Sethi, P. Strobl, and S. Domisch, "Geomorpho90m, empirical evaluation and accuracy assessment of global high-resolution geomorphometric layers," *Sci Data*, vol. 7, no. 1, May 2020, Art. no. 162.
[61] E. Uuemaa, S. Ahi, B. Montibeller, M. Muru, and A. Kmoch, "Vertical accuracy of freely available global digital elevation models (ASTER, AW3D30, MERIT, TanDEM-X, SRTM, and NASADEM)," *Remote Sens.*, vol. 12, no. 21, Oct. 2020, Art. no. 3482.
[62] L. A. Eberhard et al., "Intercomparison of photogrammetric platforms for spatially continuous snow depth mapping," *Cryosphere*, vol. 15, no. 1, pp. 69–94, Jan. 2021.
[63] L. Magruder, A. Neuenschwander, and B. Klotz, "Digital terrain model elevation corrections using space-based imagery and ICESat-2 laser altimetry," *Remote Sens. Environ.*, vol. 264, Oct. 2021, Art. no. 112621.
[64] B. H. Carlisle, "Modelling the spatial distribution of DEM error," *Trans. GIS*, vol. 9, no. 4, pp. 521–540, Oct. 2005.
[65] C. Rolstad, T. Haug, and B. Denby, "Spatially integrated geodetic glacier mass balance and its uncertainty based on geostatistical analysis: Application to the western svartisen ice cap, norway," *J. Glaciol*., vol. 55, no. 192, pp. 666–680, 2009.
[66] L. Girod, C. Nuth, A. Kääb, R. McNabb, and O. Galland, "MMASTER: Improved ASTER DEMs for elevation change monitoring," *Remote Sens.*, vol. 9, no. 7, Jul. 2017, Art. no. 704.
[67] ISO (International Organisation for Standardisation), ISO 5725-1: 1994: Accuracy (Trueness and Precision) of Measurement Methods and Results-Part 1: General Principles and Definitions. Geneva: ISO, 1994.
[68] L. Guan, H. Pan, S. Zou, J. Hu, X. Zhu, and P. Zhou, "The impact of horizontal errors on the accuracy of freely available digital elevation models (DEMs)," *Int. J. Remote Sens*., vol. 41, no. 19, pp. 7383–7399, Oct. 2020.
[69] S. Mukherjee, P. K. Joshi, S. Mukherjee, A. Ghosh, R. D. Garg, and A. Mukhopadhyay, "Evaluation of vertical accuracy of open source digital elevation model (DEM)," *Int. J. Appl. Earth Obs. Geoinf*., vol. 21, pp. 205–217, Apr. 2013.
[70] S. A. Kulp and B. H. Strauss, "New elevation data triple estimates of global vulnerability to sea-level rise and coastal flooding," *Nat. Commun*., vol. 10, no. 1, Oct. 2019, Art. no. 4844.
[71] A. Gruber, B. Wessel, M. Huber, and A. Roth, "Operational TanDEM-X DEM calibration and first validation results," *ISPRS J. Photogramm. Remote Sens*., vol. 73, pp. 39–49, Sep. 2012.
[72] A. Dehecq, R. Millan, E. Berthier, N. Gourmelen, E. Trouvé, and V. Vionnet, "Elevation changes inferred from TanDEM-X data over the Mont-Blanc area: Impact of the X-Band interferometric bias," *IEEE J. Sel. Topics Appl. Earth Observ. Remote Sens.*, vol. 9, no. 8, pp. 3870–3882, Aug. 2016.
[73] P. J. Besl and N. D. McKay, "A method for registration of 3-D shapes," *IEEE Trans. Pattern Anal. Mach. Intell*., vol. 14, no. 2, pp. 239–256, Feb. 1992.
[74] A. Myronenko and X. Song, "Point set registration: Coherent point drift," *IEEE Trans. Pattern Anal. Mach. Intell*., vol. 32, no. 12, pp. 2262–2275, Dec. 2010.
[75] Q.-Y. Zhou, J. Park, and V. Koltun, "Fast global registration," in Computer Vision - ECCV 2016. Berlin Germany: Springer, 2016, pp. 766–782.
[76] T. Zhang and M. Cen, "Robust DEM co-registration method for terrain changes assessment using least trimmed squares estimator," *Adv. Space Res*., vol. 41, no. 11, pp. 1827–1835, Jan. 2008.
[77] C. Nuth and Kääb, "Co-registration and bias corrections of satellite elevation data sets for quantifying glacier thickness change," *Cryosphere*, vol. 5, no. 1, pp. 271–290, 2011.
[78] M.-J. Noh and I. M. Howat, "Automated coregistration of repeat digital elevation models for surface elevation change measurement using geometric constraints," *IEEE Trans. Geosci. Remote Sens*., vol. 52, no. 4, pp. 2247–2260, Apr. 2014.
[79] J. B. Abshire et al., "Geoscience laser altimeter system (GLAS) on the ICESat mission: On-orbit measurement performance," *Geophys. Res. Lett*., vol. 32, no. 21, 2005, Art. no. L21S02.
[80] W. Abdalati et al., "The ICESat-2 laser altimetry mission," *Proc. IEEE*, vol. 98, no. 5, pp. 735–751, May 2010.
[81] J. Vaze, J. Teng, and G. Spencer, "Impact of DEM accuracy and resolution on topographic indices," *Environ. Model. & Softw.*, vol. 25, no. 10, pp. 1086–1098, Oct. 2010.

[82] J. Gardelle, E. Berthier, and Y. Arnaud, "Impact of resolution and radar penetration on glacier elevation changes computed from DEM differencing," *J. Glaciol.*, vol. 58, no. 208, pp. 419–422, 2012.

[83] J. Dall, S. N. Madsen, K. Keller, and R. Forsberg, "Topography and penetration of the greenland ice sheet measured with airborne SAR interferometry," *Geophys. Res. Lett.*, vol. 28, no. 9, pp. 1703–1706, May 2001.

[84] J. Li et al., "Investigating the bias of TanDEM-X digital elevation models of glaciers on the tibetan plateau: Impacting factors and potential effects on geodetic mass-balance measurements," *J. Glaciol.*, vol. 67, no. 264, pp. 613–626, Aug. 2021.

[85] F. Ackermann, "Digital image correlation: Performance and potential application in photogrammetry," *Photogramm. Rec.*, vol. 11, no. 64, pp. 429–439, Oct. 1984.

[86] R. M. Goldstein, H. A. Zebker, and C. L. Werner, "Satellite radar interferometry: Two-dimensional phase unwrapping," *Radio Sci.*, vol. 23, no. 4, pp. 713–720, Jul. 1988.

[87] H. Lee and J. G. Liu, "Analysis of topographic decorrelation in SAR interferometry using ratio coherence imagery," *IEEE Trans. Geosci. Remote Sens.*, vol. 39, no. 2, pp. 223–232, Feb. 2001.

[88] A. Wehr and U. Lohr, "Airborne laser scanning–an introduction and overview," *ISPRS J. Photogramm. Remote Sens.*, vol. 54, no. 2/3, pp. 68–82, Jul. 1999.

[89] F. J. Aguilar and J. P. Mills, "Accuracy assessment of lidar-derived digital elevation models," *Photogramm. Rec.*, vol. 23, no. 122, pp. 148–169, Jun. 2008.

[90] F. J. Aguilar, J. P. Mills, J. Delgado, M. A. Aguilar, J. G. Negreiros, and J. L. Pérez, "Modelling vertical error in LiDAR-derived digital elevation models," *ISPRS J. Photogramm. Remote Sens.*, vol. 65, no. 1, pp. 103–110, Jan. 2010.

[91] P. V. Bolstad and T. Stowe, "An evaluation of DEM accuracy: Elevation, slope, and aspect," *Photogrammetric Eng. Remote Sens.*, vol. 60, no. 11, pp. 1327–1332, 1994.

[92] Y. Gyasi-Agyei, G. Willgoose, and F. P. De Troch, "Effects of vertical resolution and map scale of digital elevation models on geomorphological parameters used in hydrology," *Hydrol. Process.*, vol. 9, no. 3/4, pp. 363–382, Apr. 1995.

[93] K. W. Holmes, O. A. Chadwick, and P. C. Kyriakidis, "Error in a USGS 30-meter digital elevation model and its impact on terrain modeling," *J. Hydrol.*, vol. 233, no. 1, pp. 154–173, Jun. 2000.

[94] T. Toutin, "Three-dimensional topographic mapping with ASTER stereo data in rugged topography," *IEEE Trans. Geosci. Remote Sens.*, vol. 40, no. 10, pp. 2241–2247, 2002.

[95] J. M. Wheaton, J. Brasington, S. E. Darby, and D. A. Sear, "Accounting for uncertainty in DEMs from repeat topographic surveys: Improved sediment budgets," *Earth Surf. Processes Landforms 35*, pp. 136–156, 2010.

[96] D. J. Milan, G. L. Heritage, A. R. G. Large, and I. C. Fuller, "Filtering spatial error from DEMs: Implications for morphological change estimation," *Geomorphology*, vol. 125, no. 1, pp. 160–171, Jan. 2011.

[97] A. Bouillon, M. Bernard, P. Gigord, A. Orsoni, V. Rudowski, and A. Baudoin, "SPOT 5 HRS geometric performances: Using block adjustment as a key issue to improve quality of DEM generation," *ISPRS J. Photogramm. Remote Sens.*, vol. 60, no. 3, pp. 134–146, May 2006.

[98] I. Dussaillant, E. Berthier, and F. Brun, "Geodetic mass balance of the northern patagonian icefield from 2000 to 2012 using two independent methods," *Front Earth Sci.*, vol. 6, 2018, Art. no. 8.

[99] R. Perko, H. Raggam, and P. M. Roth, "Mapping with Pléiades–End-to-End workflow," *Remote Sens.*, vol. 11, no. 17, Sep. 2019, Art. no. 2052.

[100] G. Falorni, "Analysis and characterization of the vertical accuracy of digital elevation models from the shuttle radar topography mission," *J. Geophys. Res.*, vol. 110, no. F2, 2005, Art. no. F02005, doi: 10.1029/2003JF000113.

[101] M. Simard, M. Neumann, and S. Buckley, "Validation of the new SRTM digital elevation model (NASADEM) with ICESAT/GLAS over the united states," in *Proc. IEEE Int. Geosci. Remote Sens. Symp.*, 2016, pp. 3227–3229.

[102] J. M. C. Belart et al., "Winter mass balance of drangajökull ice cap (NW iceland) derived from satellite sub-meter stereo images," *Cryosphere*, vol. 11, no. 3, pp. 1501–1517, Jun. 2017.

[103] L. Girod, N. I. Nielsen, F. Couderette, C. Nuth, and A. Kääb, "Precise DEM extraction from svalbard using 1936 high oblique imagery," *Geosci. Instrum. Methods Data Syst.*, vol. 7, no. 4, pp. 277–288, Oct. 2018.

[104] W. Gheyle, J. Bourgeois, R. Goossens, and K. Jacobsen, "Scan problems in digital CORONA satellite images from USGS archives," *Photogrammetric Eng. Remote Sens.*, vol. 77, no. 12, pp. 1257–1264, 2011.

[105] J. Li et al., "Early 21st century glacier thickness changes in the central tien shan," *Remote Sens. Environ.*, vol. 192, pp. 12–29, Apr. 2017.

[106] M. S. Hamid and M. Safy, "InSAR image denoising filter for accurate DEM generation," in *Proc. 12th Int. Conf. Elect. Eng.*, 2020, pp. 306–310.

[107] L. Bopche and P. P. Rege, "Use of noise reduction filters on stereo images for improving the accuracy and quality of the digital elevation model," *JARS*, vol. 15, no. 1, Feb. 2021, Art. no. 0 14508.

[108] T. Ai and J. Li, "A DEM generalization by minor valley branch detection and grid filling," *ISPRS J. Photogramm. Remote Sens.*, vol. 65, no. 2, pp. 198–207, Mar. 2010.

[109] T. Smith, A. Rheinwalt, and B. Bookhagen, "Determining the optimal grid resolution for topographic analysis on an airborne lidar dataset," *Earth Surf. Dynam.*, vol. 7, no. 2, pp. 475–489, May 2019.

[110] J. D. Wood and P. F. Fisher, "Assessing interpolation accuracy in elevation models," *IEEE Comput. Graph. Appl.*, vol. 13, no. 2, pp. 48–56, Mar. 1993.

[111] J. Gao, "Resolution and accuracy of terrain representation by grid DEMs at a micro-scale," *Int. J. Geogr. Inf. Sci.*, vol. 11, no. 2, pp. 199–212, Mar. 1997.

[112] A. G. Journel and C. J. Huijbregts, *Mining geostatistics*. Cambridge, MA, USA: Academic press London, 1978, vol. 600.

[113] N. A. C. Cressie, *Statistics for spatial data*. Hoboken, NJ, USA: Wiley, 1993, vol. 4.

[114] C. R. Ehlschlaeger and A. Shortridge, "Modeling elevation uncertainty in geographical analyses," in *Proc. Int. Symp. Spatial Data Handling*, Delft, Netherlands B, 1996, vol. 9, pp. 15–9B.

[115] P. C. Kyriakidis, A. M. Shortridge, and M. F. Goodchild, "Geostatistics for conflation and accuracy assessment of digital elevation models," *Int. J. Geogr. Inf. Sci.*, vol. 13, no. 7, pp. 677–707, Oct. 1999.

[116] S. P. Wechsler, "Digital elevation model (DEM) uncertainty: Evaluation and effect on topographic parameters," in *Proc. ESRI User Conf.*. ecn.purdue.edu, 1999, pp. 1081–1090.

[117] P. Goovaerts, *Geostatistics for Natural Resources Evaluation*. Oxford, U.K.: Oxford Univ. Press, 1997.

[118] G. B. M. Heuvelink, *Error propagation in environmental modelling with GIS*. Boca Raton, FL, USA: CRC press, 1998.

[119] A. Shortridge, "Characterizing uncertainty in digital elevation models," in *Spatial Uncertainty Ecol.: Implic. Remote Sens. GIS Appl.*, C. T. Hunsaker, M. F. Goodchild, M. A. Friedl, and T. J. Case, Eds. Berlin Germany: Springer New York, 2001, pp. 238–257.

[120] G. Wang, G. Z. Gertner, S. Fang, and A. B. Anderson, "A methodology for spatial uncertainty analysis of remote sensing and GIS products," *Photogrammetric Eng. Remote Sens.*, vol. 71, no. 12, pp. 1423–1432, 2005.

[121] G. B. M. Heuvelink, P. A. Burrough, and A. Stein, "Propagation of errors in spatial modelling with GIS," *Int. J. Geographical Inf. Syst.*, vol. 3, no. 4, pp. 303–322, Oct. 1989.

[122] P. F. Fisher, "First experiments in viewshed uncertainty: The accuracy of the viewshed area," *Photogramm. Eng. Remote Sens.*, vol. 57, no. 10, pp. 1321–1327, 1991.

[123] S. Openshaw, M. Charlton, and S. Carver, "Error propagation: A monte carlo simulation," in *Handling geographical information: methodology and potential applications*. Masser and M. Blakemore, Eds., New York USA: Wiley, Essex, 1991, pp. 102–114.

[124] F. Heße, V. Prykhodko, S. Schlüter, and S. Attinger, "Generating random fields with a truncated power-law variogram: A. comparison of several numerical methods," *Environ. Modelling Softw.*, vol. 55, pp. 32–48, May 2014.

[125] F. Canters, W. D. Genst, and H. Dufourmont, "Assessing effects of input uncertainty in structural landscape classification," *Int. J. Geogr. Inf. Sci.*, vol. 16, no. 2, pp. 129–149, Mar. 2002.

[126] S. P. Wechsler and C. N. Kroll, "Quantifying DEM uncertainty and its effect on topographic parameters," *Photogrammetric Eng. Remote Sens.*, vol. 72, no. 9, pp. 1081–1090, 2006.

[127] E. Magnússon, J. Muñoz-Cobo Belart, F. Pálsson, H. ágústsson, and P. Crochet, "Geodetic mass balance record with rigorous uncertainty estimates deduced from aerial photographs and lidar data - case study from drangajökull ice cap, NW iceland," The Cryosphere, vol. 10, no. 1, pp. 159–177, Jan. 2016.

[128] A. Bachmann and B. Allgöwer, "Uncertainty propagation in wildland fire behaviour modelling," *Int. J. Geogr. Inf. Sci.*, vol. 16, no. 2, pp. 115–127, Mar. 2002.

[129] M. Albani, B. Klinkenberg, D. W. Andison, and J. P. Kimmins, "The choice of window size in approximating topographic surfaces from digital elevation models," *Int. J. Geogr. Inf. Sci.*, vol. 18, no. 6, pp. 577–593, Sep. 2004.

[130] C. Li, Q. Wang, W. Shi, and S. Zhao, "Uncertainty modelling and analysis of volume calculations based on a regular grid digital elevation model (DEM)," *Comput. Geosci.*, vol. 114, pp. 117–129, May 2018.
[131] C. Li, S. Zhao, Q. Wang, and W. Shi, "Uncertainty modeling and analysis of surface area calculation based on a regular grid digital elevation model (DEM)," *Int. J. Geogr. Inf. Sci.*, vol. 32, no. 9, pp. 1837–1859, Sep. 2018.
[132] S. W. Anderson, "Uncertainty in quantitative analyses of topographic change: Error propagation and the role of thresholding," *Earth Surf. Processes Landforms*, vol. 44, no. 5, pp. 1015–1033, 2019.
[133] G. B. M. Heuvelink, "Analysing uncertainty propagation in GIS: Why is it not that simple?," in *Uncertainty in Remote Sensing and GIS*. Hoboken, NJ, USA:John Wiley & Sons, Ltd, Jul. 2006, pp. 155–165.
[134] R. A. Beyer, O. Alexandrov, and S. McMichael, "The ames stereo pipeline: NASA's open source software for deriving and processing terrain data," *Earth Space Sci.*, vol. 5, no. 9, pp. 537–548, Sep. 2018.
[135] NASA/METI/AIST/Japan Spacesystems, and U.S. Japan ASTER Science Team, "ASTER level 1A data set - Reconstructed, unprocessed instrument data," NASA EOSDIS Land Processes DAAC., 2001. Accessed: Jan. 1, 2019. [Online]. Available: https://doi.org/10.5067/ASTER/AST_L1A.003
[136] E. Rupnik, M. Daakir, and M. Pierrot Deseilligny, "MicMac - A free, open-source solution for photogrammetry," *Open Geospatial Data, Softw. Standards*, vol. 2, no. 1, 2017, Art. no. 17.
[137] NASA JPL, "NASA SRTM-only height and height precision global 1 arc second V001 [Data set]," *NASA EOSDIS Land Processes DAAC.*, 2020. Accessed: Jul. 12 2022. [Online]. Available: https://doi.org/10.5067/MEaSUREs/NASADEM/NASADEM_SHHP.001
[138] M.-J. Noh and I. M. Howat, "The surface extraction from TIN based search-space minimization (SETSM) algorithm," *ISPRS J. Photogramm. Remote Sens.*, vol. 129, pp. 55–76, Jul. 2017.
[139] C. Porter et al., "ArcticDEM," Nov. Harvard Dataverse, V1, 2018. Accessed: Jan. 1, 2019. [Online]. Available: https://doi.org/10.7910/DVN/OHHUKH
[140] RGI Consortium, "Randolph glacier inventory - A dataset of global glacier outlines: Version 6.0: Tech. Rep., global land ice measurements from space," colorado, USA: Digital Media, 2017. [Online]. Available: https://doi.org/10.7265/N5-RGI-60
[141] ESA, "Land cover CCI product user guide version 2. tech. rep," 2017. [Online]. Available: maps.elie.ucl.ac.be/CCI/viewer/download/ESACCI-LC-Ph2-PUGv2_2.0.pdf
[142] J. Höhle and M. Höhle, "Accuracy assessment of digital elevation models by means of robust statistical methods," *ISPRS J. Photogramm. Remote Sens.*, vol. 64, no. 4, pp. 398–406, Jul. 2009.
[143] B. K. P. Horn, "Hill shading and the reflectance map," *Proc. IEEE*, vol. 69, no. 1, pp. 14–47, Jan. 1981.
[144] L. W. Zevenbergen and C. R. Thorne, "Quantitative analysis of land surface topography," *Earth Surf. Processes Landforms*, vol. 12, no. 1, pp. 47–56, Jan. 1987.
[145] M. B. Wilk and R. Gnanadesikan, "Probability plotting methods for the analysis of data," *Biometrika*, vol. 55, no. 1, pp. 1–17, Mar. 1968.
[146] P. A. Dowd, "The variogram and kriging: Robust and resistant estimators," in *Geostatistics for Natural Resources Characterization*, G. Verly, M. David, A. G. Journel, and A. Marechal, Eds. Dordrecht, Netherlands: Springer, 1984, pp. 91–106.
[147] M. Mälicke and H. D. Schneider, "mmaelicke/scikit-gstat: A scipy flavoured geostatistical variogram analysis toolbox (v1.0.0). Zenodo," Nov. 2022. [Online]. Available: https://doi.org/10.5281/zenodo.5970098
[148] G. Matheron, "Les variables régionalisées et leur estimation: Une application de la théorie de fonctions aléatoires aux sciences de la nature," *Masson et CIE*, 1965, vol. 4597.
[149] N. Cressie and D. M. Hawkins, "Robust estimation of the variogram: I," *J. Int. Assoc. Math. Geol.*, vol. 12, no. 2, pp. 115–125, Apr. 1980.
[150] M. G. Genton, "Highly robust variogram estimation," *Math. Geol.*, vol. 30, no. 2, pp. 213–221, Feb. 1998.
[151] T. M. Burgess and R. Webster, "Optimal interpolation and isarithmic mapping of soil properties," *J. Soil Sci.*, vol. 31, no. 2, pp. 315–331, Jun. 1980.
[152] S. Müller and L. Schüler, "GeoStat-Framework/GSTools: V1.3.3 "pure pink," Zenodo, 2022. [Online]. Available: https://doi.org/10.5281/zenodo.5883346
[153] E. J. Pebesma and C. G. Wesseling, "gstat : A. program for geostatistical modelling, prediction and simulation," *Comput. Geosci.*, vol. 24, no. 1, pp. 17–31, 1998.
[154] R. Webster and M. A. Oliver, *Geostatistics for Environmental Scientists*, 2nd ed. Hoboken, NJ, USA: Wiley, Nov. 2007.
[155] H. Liu and K. C. Jezek, "Investigating DEM error patterns by directional variograms and fourier analysis," *Geogr. Anal.*, vol. 31, no. 3, pp. 249–266, Sep. 2010.
[156] E. Rodríguez, C. S. Morris, and J. E. Belz, "A global assessment of the SRTM performance," *Photogrammetric Eng. Remote Sens.*, vol. 72, no. 3, pp. 249–260, 2006.
[157] xdem contributors, "xdem (v0.0.2)," May 2021. [Online]. Available: https://doi.org/10.5281/zenodo.4809698

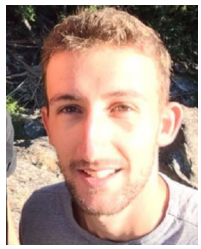

Romain Hugonnet received the M.Sc. degree in engineering and in mechanics from Ecole Centrale de Lille, Villeneuve-d'Ascq, France, in 2017.

Since 2018, he has been working as a Ph.D. student for the Laboratory for Space Studies in Geophysics and Oceanography, Toulouse, France and the Laboratory of Hydraulics, Hydrology and Glaciology, ETH Zürich, Switzerland. His research aims at monitoring the Earth system by remote sensing, with a focus on glaciology and digital elevation models. His fields of expertise are satellite imagery and spatiotemporal analyses, including uncertainty quantification.

Fanny Brun received the Ph.D. degree in earth sciences from the University Grenoble Alpes, Grenoble, France, in 2018.

Since 2020, she has been working with IRD in the Institute of Environmental Geosciences, Grenoble, France. She currently serves as Scientific Editor for the *Journal of Glaciology*. Her research aims at observing glacier changes from remote sensing and field techniques, with a focus in Asia.

Etienne Berthier received the Ph.D. degree in glaciology and remote sensing from the University of Toulouse, Toulouse, France, in 2005.

Since 2007, he has been working with CNRS in the Laboratory for Space Studies in Geophysics and Oceanography, Toulouse, France. His field of expertise is satellite remote sensing, including the retrieval of ice topography from optical images to measure ice elevation changes. He currently serves as the Scientific Editor for *The Cryosphere* and *La Météorologie* (in French). His research aims at observing and understanding the effect of climate change on mountain glaciers and ice caps and quantifying their contribution to sea level rise.

Dr. Berthier is member of the European Geophysical Union and the International Glaciological Society.

Amaury Dehecq received the Ph.D. degree in remote sensing from the University Grenoble Alpes, Grenoble, France, in 2015.

From 2019 to 2021, he worked as a Postdoctoral Researcher with ETH Zurich's Laboratory of Hydraulics, Hydrology and Glaciology (VAW). Since 2021, he has been working with the French National Research Institute for Sustainable Development (IRD) and based at the Institute for Geosciences and Environmental research (IGE), Grenoble, France. His research focuses on estimating 20th century mountain glacier changes from remote sensing observations, using a combination of modern satellite, declassified spy satellite, and historical airborne/terrestrial images.

Erik Schytt Mannerfelt received the M.Sc. degree in geology from UiT — The Arctic University of Norway, Troms, Norway, in 2020.

Between 2020 and 2022, he has worked with the Laboratory of Hydraulics, Hydrology and Glaciology, ETH Zurich, Switzerland, as a Research Assistant. His research focuses on fieldwork-, modelling-, and photogrammetry-based methods to constrain late Little Ice Age to contemporary glacier change and dynamics.

Nicolas Eckert received the Ph.D. degree in environmental statistics from AgroParisTech, Paris, France, in 2007.

Since 2008, he has been a Researcher with INRAE Grenoble, and has been an co-head of the mountain risk team since 2018. He is also Task Officer in charges of environmental risks for the AQUA department with INRAE, and for the ALLENVI research federation. He serves as an Associate Chief Editor for *Journal of Glaciology* and as Scientific Editor for *Cold Regions Science and Technology*. His research is at the crossroads between geosciences and statistical modelling, with applications to mountain risks, mountain climatology and glaciers. Additional interests in the socio-historical component of risk makes him involved in interdisciplinary research addressing all dimensions of mountain risks.

Daniel Farinotti received the doctoral degree in glaciology from the Swiss Federal Institute of Technology in Zurich (ETH Zurich), Switzerland, in 2010.

Since 2016 he leads the Professorship of Glaciology with ETH Zurich's Laboratory of Hydraulics, Hydrology and Glaciology (VAW), a position jointly affiliated to the Swiss Federal Institute for Forest, Snow and Landscape Research WSL. His research focuses on the evolution of glaciers and the implications for water resources, notably including the estimation of glacier ice thickness from surface characteristics, the long-term modelling of glacier mass budgets, the estimation of the runoff contributions from glacierized catchments, or the implications for water resource management in high-mountain environments.